Nuclear RNAi Modulates Influenza A Virus Infectivity By Downregulating Type-I Interferon Response

Hsiang-Chi Huang[1,2,3,#], Iwona Nowak[1,2], Vivian Lobo[1,2], Danica F. Besavilla[3,], Karin Schön[3], Jakub O. Westholm[4], Carola Fernandez[1,2], Angana A.H. Patel[2,5], Clotilde Wiel[5], Volkan I. Sayin[2,5], Dimitrios G. Anastasakis[6], Davide Angeletti[3,7§,#] and Aishe A. Sarshad[1,2,§,#]

1 Department of Medical Biochemistry and Cell Biology, Institute of Biomedicine, University of Gothenburg, SE-40530 Gothenburg, Sweden

2 Wallenberg Centre for Molecular and Translational Medicine, University of Gothenburg, SE-40530 Gothenburg, Sweden

3 Department of Microbiology and Immunology, Institute of Biomedicine, University of Gothenburg, SE-40530 Gothenburg, Sweden

4 Dept of Biochemistry and Biophysics, National Bioinformatics Infrastructure Sweden, Science for Life Laboratory, Stockholm University, Box 1031, SE-17121 Solna, Sweden

5 Department of Surgery, Institute of Clinical Sciences, Sahlgrenska Center for Cancer Research, University of Gothenburg, SE-40530 Gothenburg, Sweden

6 RNA Molecular Biology Laboratory, National Institute for Arthritis and Musculoskeletal and Skin Disease, Bethesda, MD 20892, USA.

7 SciLifeLab, University of Gothenburg, SE-40530 Gothenburg, Sweden

[§] Joint senior authors

[#] Correspondence to hsiang-chi.huang@gu.se, davide.angeletti@gu.se, aishe.sarshad@gu.se

Keywords: Argonaute 2; nuclear RNAi; influenza A virus; NS1; p53; Tp53 KO mice; Arsenic trioxide (ATO); type-I interferons; fPAR-CLIP; TRIM71

ABSTRACT

The role of Argonaute (AGO) proteins and the RNA interference (RNAi) machinery in mammalian antiviral response has been debated. Therefore, we set out to investigate how mammalian RNAi impacts influenza A virus (IAV) infection. We reveal that IAV infection triggers nuclear accumulation of AGO2, which is directly facilitated by p53 activation. Mechanistically, we show that IAV induces nuclear AGO2 targeting of TRIM71, a proposed AGO2 E3 ligase, and type-I interferon-pathway genes for silencing. Accordingly, *Tp53*$^{-/-}$ mice do not accumulate nuclear AGO2 and demonstrate decreased susceptibility to IAV infection. Hence, the RNAi machinery is highjacked by the virus to evade the immune system and support viral replication. Furthermore, the FDA approved drug arsenic trioxide, which prevents p53 tetramerization and nuclear translocation, increases interferon response and decreases viral replication *in vitro* and in a mouse model *in vivo*. Our data indicates that targeting the AGO2:p53-mediated silencing of innate immunity may offer a promising strategy to mitigate viral infections.

INTRODUCTION

Argonaute (AGO) proteins have a central role in RNA interference (RNAi), where they are guided by endogenous miRNA or exogenous siRNA to recognize (partially) complementary sequences on target RNAs [1]. Together, AGO-small RNA (smRNA) constitutes the core of the RNA-induced silencing complex (RISC), a multiprotein complex that deregulates RNA transcripts, resulting in target destabilization [1]. RNAi has a well-established role in antiviral defense in certain eukaryotes, including plants, insects and nematodes [2,3]. However, in mammals, the role of RNAi as an antiviral defense mechanism is more controversial: indeed, while some studies described antiviral RNAi functions [4,5], many others reported a lack of evidence for direct antiviral activity [6]. What has not been extensively investigated is whether RNAi could be hijacked by viruses to their advantage. Sparse evidence suggests that loss of RNAi after viral infection may indeed decrease viral titers with concomitant increased expression of antiviral genes [6-8]. The overall picture and detailed mechanisms of action remain, however, elusive.

Upon infection with influenza A virus (IAV), the innate immune system serves as the body's primary defense, swiftly initiating a response to combat invading pathogens [9]. A crucial facet of the innate immune response to IAV is the synthesis of type-I interferons (IFN-Is) by infected cells. These interferons subsequently activate neighboring cells to produce antiviral proteins, which are essential in curtailing the severity and duration of infections [10]. Viral RNAs, in their single-strand or intermediate format, can be recognized by the Toll-like receptors TLR3 and TLR7 to activate IFN transcription via NF-kβ, IRF-3 or IRF-7 [9]. Collectively, viral RNAs therefore activate the immune system by different mechanisms, which all lead to interferon production. Additionally, the tripartite motif (TRIM) family of proteins modulates the production, signaling, and effector functions of IFN-Is, thereby influencing immune responses and host defense against pathogens. Notably, TRIM25, TRIM56, and TRIM71 exert positive regulatory roles in the IFN-I pathway [11].

From the IAV side, the multifunctional nonstructural protein 1 (NS1) of IAV serves as an RNA-binding protein, facilitating mRNA export from the nucleus. Moreover, unrelated to the nuclear export function, NS1 can re-enter the cell nucleus and has a pivotal role in antagonizing host immune responses and facilitating pathogenesis [12-15]. Furthermore, NS1 has been shown to inhibit TRIM25 oligomerization, thus suppressing RIG-I-mediated IFN production [16]. Therefore, NS1 is the key player in IAV innate immune evasion, with multiple functions, including the ability to block RISC ribosylation [7]. It has been shown that ribosylation

80 of the RISC complex leads to the shutdown of RNAi mechanisms. This is intriguing because
81 it suggests that it is in the virus' best interest to maintain RNAi function. However, while it
82 was shown that two specific miRNAs could inhibit interferon-stimulated genes (ISGs) in IFN-
83 treated cells, there are still open questions regarding global, mechanistic functions of RNAi
84 after viral infections.

85 Adding to the complexity of viral regulation of RISC function is the identification of
86 nuclear RNAi. In metazoans, cytoplasmic RNAi processes are well documented [17], yet the core
87 RISC components – AGOs and miRNAs – have been found in cell nuclei [18-21]. Indeed, various
88 mechanisms of stress-induced nuclear translocation of AGOs have been proposed, including
89 DNA damage and viral infection [22,23]. While cytoplasmic AGO2 is well known as a critical
90 component of RISC and is involved in siRNA/miRNA-mediated gene suppression pathways
91 [24], little is known about the specific functions of nuclear AGO2. This is particularly relevant to
92 disentangle the controversies around the role of RNAi in mammals after viral infections.

93 To comprehensively address the role of RNAi following IAV infection, we combined
94 *in vitro* and *in vivo* experimental models with fluorescence-based photoactivatable
95 ribonucleoside-enhanced crosslinking and immunoprecipitation (fPAR-CLIP) to pinpoint
96 AGO2 targets at nucleotide resolution. We demonstrate that upon IAV infection, NS1 mediates
97 AGO2 translocation into the cell nucleus to silence TRIM71 and IFN-pathway-related genes,
98 thereby increasing viral replication. Our data provide important mechanistic insights into
99 previously underappreciated modalities of viral resistance.
100

101 **RESULTS**

102 **Viral infection induces nuclear accumulation of AGO2**

103 AGO2 may localize both in the cytoplasm and the nucleus of human cells [25]. For instance, we
104 previously demonstrated the absence of nuclear AGO2 in HEK293 cells [21,25]. However, we
105 observed a high degree of nuclear AGO2 in HEK293T cells, which are HEK293 cells
106 transformed with SV40 large T (LT) antigen, the master regulator of polyomaviruses [26] (**Fig**
107 **1A**). Biochemical fractionation of HEK293T cells showed a near 50-50 distribution of AGO2
108 between the cytoplasmic and nuclear fractions (**Fig 1A**). Moreover, transient overexpression
109 of SV40 LT antigen in HEK293 cells led to the translocation of AGO2 into the nucleus (**Fig**
110 **1B**), indicating the involvement of SV40 LT antigen in AGO2 nuclear accumulation. These
111 observations prompted us to investigate whether nuclear translocation of AGO2 is shared by
112 acute viral infections.

113 To address this, we took advantage of PR8 strain of IAV as a model system. PR8 is
114 favored in IAV research for its well-defined genetics, ease of modification, availability of
115 mutants and ability to infect mice [27]. HEK293 cells were infected with PR8-IAV at several
116 multiplicity of infection (MOI) for 16 hours, and biochemical fractionation experiments were
117 performed (**Fig 1C**). We observed robust nuclear translocation of AGO2 upon infection with
118 PR8-IAV, particularly at MOI 2 or higher (**Fig 1C**). MOI lower than 2 did not yield any nuclear
119 translocation of AGO2 after 16 hours of infection, suggesting that MOI < 2 may need longer
120 time of infection. However, IAV infection must be performed in serum-free media which, by
121 itself, induced cellular stress and AGO2 nuclear translocation (**Sup Fig 1A**). Therefore, all
122 subsequent experiments were conducted at 16 hours of viral infection at MOI 2 or 10. Under
123 these conditons, we also observed the nuclear translocation of AGO1 and AGO3 proteins upon
124 viral infection (**Fig 1D**), suggesting that the nuclear accumulation of RNAi factors is a general
125 phenomenon during IAV infection. To visualize the nuclear accumulation of AGO2 upon viral
126 infection, we utilized a fluorescently tagged PR8 virus strain, which has mCherry inserted
127 within the NS1 protein [28], and performed confocal microscopy (**Fig 1E, Sup Fig 1B**).

128 IAV consists of eight gene segments that encode up to 17 viral proteins [29]. To identify
129 the specific gene segment responsible for AGO2 nuclear accumulation, we transiently
130 expressed each influenza protein in HEK293 cells and performed biochemical fractionation
131 assays. Interestingly, we found that NS1 is the primary viral factor triggering AGO2 nuclear
132 translocation (**Fig 1F**). NS1 has a N-terminal RNA binding domain, containing an NLS signal,
133 and a C-terminal effector domain, interacting with cellular signals and regulating their
134 functions [30]. Furthermore, the first 113 amino acids are sufficient for normal RNA binding

135 activity [31]. The effector domain, comprising amino acid residues 86-205, is crucial for its
136 function [32]. Therefore we generated two NS1 truncated mutants and demonstrated that NS1-
137 effector domain was indeed responsible for the nuclear translocation of AGO2 (**Fig 1G**).
138 Furthermore, we observed nuclear co-localization of AGO2 with NS1 after transient expression
139 of mCherry-tagged NS1 protein (**Fig 1H, Sup Fig 1C**). Collectively, these findings suggest
140 that viral proteins, including SV40 LT antigen and IAV NS1, induce nuclear accumulation of
141 AGO1-4.
142
143 **AGO2 interacts with p53 in the nucleus upon viral infection**
144 Having established the nuclear translocation of AGO2, after IAV infection, we next wanted to
145 identify potential interacting partners of AGO2 involved in its translocation or stabilization.
146 Therefore, we retrieved a list of AGO2-associated proteins (**Sup Table 1**) from the
147 Harmonizome database [33], and performed a protein-protein interaction network analysis by
148 STRING (**Fig 2A**). STRING aggregates diverse data to map protein-protein interactions,
149 enhancing understanding of molecular functions and cellular processes. We identified that
150 AGO2 directly interacts with p53, as well as with other well-known components of the RISC
151 complex (**Fig 2A**). Interestingly, SV40 LT antigen also possesses a p53 binding domain [34],
152 Therefore, we wondered whether p53 may play a role in the nuclear translocation of AGO2
153 after IAV infection and whether p53 can also interact with the NS1 component of IAV.
154 To address these questions, we first examined the subcellular localization of p53 in
155 HEK293 cells. We observed that p53 levels are low, yet ubiquitous, in HEK293 cells but, as
156 reported, the majority of p53 translocated into the nucleus when cells were treated with
157 doxorubicin, a DNA damage-inducing agent, for 24 hours (**Fig 2B**) [35]. Consistent with our
158 hypothesis, AGO2 also translocated into the nucleus in doxorubicin-treated cells (**Fig 2B**).
159 Furthermore, by performing a co-immunoprecipitation experiment, we demonstrated a direct
160 interaction between AGO2 and p53 upon doxorubicin treatment (**Fig 2C**). Interestingly, in lung
161 cancer cells A549 (**Sup Fig 2A**), HEK293T (**Sup Fig 2B**), neuroblastomas cells SK-N-BE(2)
162 (**Sup Fig 2C**) and breast cancer cell line MCF7 (**Sup Fig 2D**) AGO2 and p53 are ubiquitously
163 expressed but interact exclusively within the nucleus (**Sup Fig 2A-D**).
164 Next, we investigated the subcellular localization of p53 in response to transient
165 expression of SV40 LT antigen (**Fig 2D**) and NS1 (**Fig 2E and Sup Fig 2E**). Indeed,
166 overexpression of both viral proteins induced substantial translocation of p53 into the nucleus,
167 together with AGO2 (**Fig 2D,E**). Furthermore, in IAV-infected HEK293 cells, we observed
168 not only nuclear AGO2 but also nuclear p53 accumulation (**Fig 2F**). Finally, to test whether

169 AGO2 and p53 interact with each other also in response to viral infection, we co-
170 immunoprecipitated AGO2 with p53. Indeed, we observed an interaction between AGO2 and
171 p53 in virus-infected cells but not in control cells (**Fig 2G**). Similarly, we found that p53:AGO2
172 co-immunoprecipitated after transient expression of either SV40 LT (**Fig 2H**) or NS1 antigen
173 (**Fig 2I**) but not NS1 mutant (**Sup Fig 2F**).
174 Taken together, our findings suggest that both AGO2 and p53 translocate into the
175 nucleus where they interact with each other in response to IAV infection. Furthermore, in cells,
176 such as A549, which already have nuclear AGO2, p53 and AGO2 interact, indicating a
177 potential functional interplay between these two proteins in the nucleus.
178
179 **The N-terminus of tetrameric p53 interacts with AGO2 and protects AGO2 from**
180 **proteasomal degradation in the nucleus.**
181 We next wanted to examine how AGO2:p53 interact and what functional outcome the
182 interaction may have in the nucleus. p53 is a 53 kDa protein consisting of an N-terminal
183 transactivation domain, proline-rich domain, a core DNA binding domain and a C-terminal
184 tetramerization and regulatory domain [36] (**Fig 3A**). The PIWI domain of AGO2 contains
185 tandem tryptophan-binding pockets, which collectively form a region for interacting with
186 TNRC6 or other tryptophan-rich cofactors [37,38]. Interestingly, we observed the presence of three
187 tryptophan residues (Trp23, Trp53, and Trp91) within the flexible N-terminal loop region of
188 p53 (**Sup Fig 3A**), suggesting that the N-terminus may be involved in AGO2 binding. To
189 investigate the possible interaction between the N-terminal region of p53 and AGO2, we
190 generated two Flag-p53 mutants by removing amino acids 1-61 and 1-92 from the N-terminus
191 (**Fig 3B**). Upon transient overexpression of these mutants in doxorubicin-treated HEK293
192 cells, we found that AGO2 exclusively interacts with full-length Flag-p53, while the interaction
193 was abolished in both N-terminal mutants (**Fig 3C**).
194 Activated p53 tetramerizes in the nucleus [39] and therefore we next wanted to test if the
195 tetrameric form is essential to interact with AGO2. In SK-N-BE(2) cells, known to possess
196 intact *TP53* transcriptional activity, AGO2:p53 interacts in the nucleus (**Sup Fig 2C**) [40]. To
197 explore the effect of p53 monomerization, we treated SK-N-BE(2) cells with increasing
198 concentrations of arsenic trioxide (ATO), a known inducer of p53 monomerization, for 24
199 hours [41]. Remarkably, we observed a significant reduction in nuclear p53 localization with 0.1
200 μg/ml ATO treatment, and complete displacement of nuclear p53 at 0.5 μg/ml (**Sup Fig 3B**).
201 Strikingly, AGO2 was also displaced from the nucleus upon treatment with 0.5 μg/ml ATO
202 (**Sup Fig 3B**). Similar results were observed in A549 lung carcinoma cells (**Fig 3D**), HEK293T

203 (**Sup Fig 3C**) and MCF7 breast cancer cells (**Sup Fig 3D**), where nuclear AGO2 and p53
204 accumulate in the cytoplasm after ATO treatment. Being able to manipulate p53 into its
205 monomeric state, we next examined whether AGO2:p53 can interact under these conditions.
206 Consequently, we performed co-immunoprecipitation assays in the above-mentioned cell lines,
207 using whole cell lysates, in the presence or absence of ATO, and found that ATO-mediated
208 monomerization of p53 reduces its capability to interact with AGO2 (**Fig 3E, Sup Fig 3E,F**),
209 highly suggestive of the fact that p53 and AGO2 only interact in the nucleus.

210 Since the PIWI domain of AGO2 interacts with both p53 and TNRC6 at tryptophan-
211 rich regions [37], we next investigated if these interactions are mutually exclusive. Therefore we
212 docked the PIWI domain with the T6B region of TNRC6B and N-terminal region of p53 using
213 the HDOCK server [42]. The docking results indicated that AGO2 can bind to the N-terminal
214 region of p53 and the T6B region of TNRC6 at different positions on the PIWI domain,
215 depending on structural conformation of the proteins (**Fig 3F**, **Sup Table 2**). This suggests that
216 the proteins may bind independently. To experimentally validate the computational models,
217 we performed AGO2 or p53 immunoprecipitation assay from cytoplasmic and nuclear
218 fractions of A549 cells. Our data suggest that AGO2 interacts with both p53 and TNRC6 in the
219 nuclear fraction (**Fig 3G,H**) but, as expected, exclusivly with TNRC6 in the cytoplasm (**Fig
220 3G,H**).

221 Having found a robust interaction between AGO2:p53, we next wanted to gauge for its
222 biological significance. To test whether p53 plays a role in the stability of AGO2, we silenced
223 *TP53* using siRNAs. *TP53* silencing resulted in a decrease in AGO2 protein levels in A549
224 (**Fig 3I**), MCF7 (**Sup Fig 3G**) and HEK293T cells (**Sup Fig 3H**), suggesting that p53 may
225 indeed stabilize AGO2 in the nucleus. However, silencing AGO2 in the same cells did not lead
226 to reciprocal instability of p53 (**Fig 3I, Sup Fig 3G,H**) further corroborating the specificity of
227 p53 mediated stability of AGO2. To confirm these findings, we employed p53 low-expressing
228 MCF7 cells (hereafter referred to as TP53L cells) [43]. Biochemical fractionation assays in
229 wildtype (WT) and TP53L MCF7 cells revealed a similar downregulation of AGO2 protein
230 levels, specifically in the nucleus, upon loss of p53 (**Sup Fig 3I**).

231 So far, we demonstrated that tetrameric p53 is needed for an interaction with AGO2 in
232 the nucleus, however, it remained unclear whether p53 is needed for nuclear import of AGO2
233 or to stabilize AGO2 within the nucleus. Therefore, we tested if AGO2 is degraded by the
234 ubiquitin-proteasome system when p53 is monomeric, by combining ATO treatment with the
235 proteasome inhibitor MG132. In cells treated with MG132 and ATO, we found that AGO2 co-
236 immunoprecipitated with anti-ubiquitin antibodies, indicating that AGO2 is tagged with

237 ubiquitin for proteasome degradation in the absence of nuclear p53 (**Fig 3J, Sup Fig 3J**).
238 Having previously observed that AGO1 and AGO3 also translocated into the nucleus in IAV-
239 infected cells, we performed STRING analysis and identified that p53 may form complex with
240 AGO1 and AGO2, but not with AGO3 and AGO4 (**Sup Fig 3K**). Therefore, we also evaluated
241 if AGO1 is susceptible to p53 mediated degradation. Our results revealed that AGO1 co-
242 immunoprecipitated with anti-ubiquitin antibodies in cells treated with MG132 and ATO,
243 indicating that also AGO1 is degraded in the absence of nuclear p53 (**Sup Fig 3L**).
244 Collectively, our findings demonstrate an interaction between p53 and AGO2 in the
245 nucleus, mediated by tetrameric p53. The interaction with p53 stabilizes AGO2 and protects it
246 from proteasomal degradation.
247
248 **Nuclear AGO2 facilitates viral infection**
249 Having observed a significant influx of both AGO2 and p53 into the nucleus upon viral
250 infection and that p53 stabilizes AGO2 in the nucleus, we next aimed at determining if and
251 how this phenomenon would influence viral infection. Specifically, we addressed whether
252 nuclear AGO2:p53 serves as a proviral or an antiviral mechanism. To confirm whether the lack
253 of p53 inhibits AGO2 translocation to the nucleus upon viral infection, we generated *TP53*
254 knockout (KO) HEK293 cells by CRISPR-CAS9 (**Sup Fig 4A**). HEK293 cells infected with
255 PR8-IAV at MOI 2 or MOI 10 translocated AGO2 into the nucleus (**Fig 1C, Fig 4A**), but the
256 nuclear localization of AGO2 was lost in infected TP53 KO HEK293 cells (**Fig 4A**, **Sup Fig**
257 **4B**). Similarly, in WT MCF7 cells AGO2 predominantly localized in the nucleus, regardless
258 of viral infection dose (**Sup Fig 4C**). In contrast, AGO2 remained cytoplasmic in TP53L MCF7
259 cells, irrespective of viral infection load (**Sup Fig 4D**). Furthermore, we measured viral gene
260 expression in the above mentioned cells and observed a significant reduction of viral mRNA
261 levels in TP53 KO HEK293 ad TP53L MCF7 cells (**Fig 4B, Sup Fig 4E**). To further verify
262 that RNA expression of viral genes was correlated with viral infectivity, we infected WT and
263 TP53 KO HEK293 cells, as well as WT and TP53L MCF7 cells, with PR8-mCherry virus and
264 measured mCherry expression in infected cells using flow cytometry. TP53 KO HEK293 cells
265 exhibited reduced viral replication (**Fig 4C**), which was was also evident in TP53L MCF7 cells
266 (**Sup Fig 4F**). Overall, the reduced mRNA expression of NS1 and HA observed upon viral
267 infection correlated with the lack of AGO2:p53 nuclear translocation (**Fig 4A, Sup Fig 4B-D**).
268 Finally, we investigated the reversibility of this phenomenon by overexpressing p53 in TP53
269 KO HEK293 and in TP53L MCF7 cells. p53 overexpression partially restored viral gene
270 expression (**Fig 4D, Sup Fig 4G**) and also promoted AGO2 nuclear accumulation (**Fig 4E,**

271 **Sup Fig 4H**). Our data indicated that IAV infection is facilitated through the nuclear
272 localization of AGO2:p53 complexes, however, it could not distinguish between a key role of
273 either nuclear AGO2 or p53 in mediating the proviral outcome. Therefore, to test if AGO2 is
274 essential in facilitating viral infectivity, we silenced *AGO2* in HEK293 cells by siRNAs,
275 infected the cells with IAV and finally measured the mRNA levels of viral genes by qRT-PCR.
276 It is important to consider that silencing *AGO2* did not affect the stability of nuclear p53 (**Fig**
277 **3I, Sup Fig 3G,H**). We found that mRNA levels of viral genes decreased when AGO2 was
278 silenced in WT HEK293 cells (**Fig 4F, Sup Fig 4I-K).** Our results were recapitulated in A549
279 cells where we silenced either *AGO2* or *TP53* by siRNAs upon IAV infection and found that
280 viral mRNA was significantly decreased (**Fig 4G**). Interestingly, silencing *AGO2* in TP53 KO
281 HEK293 cells, infected with PR8-IAV, did not affect the levels of HA or NS1 viral mRNAs
282 given the inability of AGO2 to translocate to the nucleus without p53 (**Sup Fig 4L**). Lastly, to
283 confirm the role of NS1, we infected HEK293 cells with either PR8 or PR8-NS1$_{1\text{-}124}$ mutant
284 and silenced either p53 or AGO2. While silencing either p53 or AGO2 resulted in reduced viral
285 mRNAs upon PR8 infection, it did not influence infectivity after PR8-NS1$_{1\text{-}124}$ mutant
286 infection, thus supporting the crucial role of NS1 (**Fig 4H,I**).
287 To summarize, we showed that mRNA levels of viral genes was similarly reduced after
288 TP53 KO and siAGO2 (which had nuclear p53) in IAV-infected HEK293 cells, thus
289 confirming an essential role for nuclear AGO2 but not p53 in the increased viral gene
290 expression. Overall, we discovered a clear link between nuclear AGO2 localization and viral
291 mRNA levels, indicating a proviral role of nuclear AGO2.
292
293 **Nuclear AGO2 downregulates antiviral type-I interferon response**
294 Upon IAV infection, innate immunity is the first line of host defense, and the immediate
295 immune response is mediated by type-I IFN. Type-I IFN are rapidly produced by infected cells
296 to trigger an antiviral state, thus inhibiting viral replication [44]. Given that AGO2:p53 nuclear
297 translocation increased viral titer, we therefore hypothesized that AGO2:p53 nuclear
298 translocation might have a proviral function by downregulating innate immune responses.
299 First, we assessed the steady state levels of IFN-Is by measuring *IFNB* mRNA levels [45] by
300 qRT-PCR in HEK293 vs HEK293T cells. Interestingly, we observed significantly higher levels
301 of *IFNB* in HEK293 cells (nuclear AGO2 negative) compared to HEK293T cells (nuclear
302 AGO2 positive) (**Fig 5A**), indicative of distinct IFN-I regulation between the two cell lines.
303 Subsequently, we examined the dynamics of *IFNB* levels in HEK293 cells at three
304 distinct time points following PR8 infection. We observed an initial increase in *IFNB* at 2 hours

305 post-infection, followed by a decrease at 8- and 16-hours post-infection, where the levels were
306 lower than baseline (**Fig 5B**). In the same time frame mentioned above, we also performed
307 biochemical fractionation assays. Strikingly, the decline in *IFNB* production coincided with
308 the translocation of AGO2 into the nucleus at 8 hours post-infection, suggesting a potential
309 contribution of nuclear AGO2 in the downregulation of antiviral IFN-I production (**Fig 5C**).
310 To explore whether the regulation of IFN-I expression is a general feature in cells
311 positive for nuclear AGO2, we measured *IFNB* in WT and TP53L MCF7 cells. Notably, we
312 observed low levels of *IFNB* expression in WT MCF7 cells (with nuclear AGO2), while the
313 TP53L MCF7 cells, lacking nuclear AGO2, displayed significantly higher *IFNB* levels (**Sup**
314 **Fig 5A**). Having observed that the lack of p53, and consequent lack of nuclear AGO2, allows
315 for the expression of *IFNB*, we next reasoned that we should be able to recapitulate the above
316 observation in nuclear AGO2 positive cells when p53 is monomeric and AGO2:p53 complex
317 is excluded from the nucleus (**Fig 3D, Sup Fig 3C,D**). To investigate the impact of p53
318 monomerization on IFN-I expression we measured *IFNB* levels in A549 and HEK293T cells
319 treated with ATO and observed a significant increase in *IFNB* (**Fig 5D, Sup Fig 5B**), which is
320 likely due to the exclusion of AGO2:p53 from the nucleus. Furthermore, as expected, A549,
321 HEK293T and MCF7 cells treated with ATO and infected with IAV exhibited reduced viral
322 gene expression (**Fig 5E, Sup Fig 5C,D**), linked with rescued *IFNB* levels (**Fig 5F, Sup Fig**
323 **5E,F**). In addition, to further elucidate the role of AGO2:p53 axis in regulating *IFNB*
324 expression, we performed siRNA-mediated knockdown of *AGO2* and *TP53* in A549 and
325 HEK293T cells and measured *IFNB* mRNA levels (**Fig 5G, Sup Fig 5G**). Silencing either
326 *AGO2* or *TP53* led to an increase in *IFNB* mRNA levels (**Fig 5G, Sup Fig 5G**). Importantly,
327 p53 nuclear localization is not compromised with AGO2 silencing (**Fig 3I, Sup Fig 3G,H**)
328 hence suggesting a direct role of nuclear AGO2 in *IFNB* regulation.
329 Type-I IFNs, which are produced by infected cells, trigger a signaling cascade that
330 timely leads to an antiviral state by promoting the expression of interferon simulating response
331 elements (ISRE), via IFNAR1 and IFNAR2 stimulation [44]. Therefore, we next wanted to gauge
332 whether increase in *IFNB* triggered downstream activation of IFNAR-mediated ISRE pathway
333 after IAV infection. Importantly, silencing of *AGO2* by siRNA resulted in a significant increase
334 of *IFNAR2* expression in HEK293 cells infected with IAV (**Fig 5H**). To assess the downstream
335 effects of interferon response, we measured the expression of ISRE. Utilizing a luciferase
336 reporter assay in both IAV-infected and control HEK293 cells, we found that the ISRE
337 expression was significantly increased in IAV-infected cells only when AGO2 was silenced
338 (**Fig 5I**). ISRE measurements in A549 (nuclear AGO2 positive) demonstrated an increase of

339 ISRE in both infected and uninfected cells, upon AGO2 silencing (**Fig 5J**). Luciferase results
340 were confirmed by qPCR that showed the upregulation of several ISRE genes in IAV-infected
341 cells upon AGO2 and TP53 silencing in both A549 and HEK293T cells (**Fig 5K, Sup Fig 5H**).
342 Taken together, our findings support the notion that nuclear localization of AGO2 acts as a
343 mechanism to suppress the induction of antiviral IFN-I and its signaling cascade, thereby
344 facilitating viral infection. This resistance mechanism utilized by viruses highlights the
345 complex interplay between viral pathogens and the host immune response.
346
347 **Type-I-IFN-pathway-related genes and *TRIM71* are negatively regulated by nuclear**
348 **RNAi.**
349 As nuclear AGO2 translocation correlated with diminished interferon expression and enhanced
350 viral gene expression, we hypothesized that nuclear RNAi may directly suppress type-I IFNs.
351 First, to comprehensively understand the transcriptional dynamics of host cellular responses
352 during IAV infection, we conducted RNA sequencing experiments in HEK293 cells post-IAV
353 infection. The results of principal component analysis (PCA) demonstrated that IAV infection
354 elicited a distinctive transcriptomic profile in HEK293 cells (**Sup Fig 6A**). Further, we
355 identified 1773 differentially upregulated and 352 differentially downregulated RNA
356 transcripts in response to IAV infection (**Sup Fig 6B** and **Sup Table 3**). As expected, gene
357 ontology (GO) analysis of biological processes revealed that PR8 infection significantly
358 induced defense response and regulation of immune effector processes (**Sup Fig 6C)**.
359 Upregulated genes, associated with inflammation and innate immunity, included *ARRD3,*
360 *ITGB1BP2, SOCS1, SOCS3, TRIM72, GADD45B,* and *CD68* (**Sup Fig 6B**). Notably, among
361 the upregulated genes, *TRIM72*, and *SOCS1* emerged as potential inhibitors of the IFN-I
362 response, with reported interactions with RIG-1, IFNB, and IFNAR, respectively [46-48]. While
363 *IFNB* itself could not be detected in the RNAseq dataset, many genes upstream of *IFNB*,
364 including *MAVS*, *IRF3*, *TRIF3*, and *TRIF6,* were downregulated.
365 To explore the role of nuclear RNAi and define AGO targets at nucleotide resolution,
366 we employed fPAR-CLIP assay [49] in two replicates in HEK293 cells with or without IAV
367 infection, from either cytoplasmic or nuclear fractions and using the T6B peptide, which
368 recognizes all four AGOs, to isolate AGO-bound RNAs [50] (**Sup Fig 6D**). Overall, we identified
369 41 743 cytoplasmic and 12 119 nuclear AGO1-4 binding sites in control cells (**Fig 6A**). At 16
370 hours post IAV infection, we identified 30 083 cytoplasmic and 78 665 nuclear AGO1-4
371 binding sites, a remarkable 6.5 fold increase of nuclear AGO-targets (**Fig 6A**). A clear
372 difference in control *vs* IAV-infected nuclear AGO target occupancy was also evident by PCA

373 analysis (**Sup Fig 6E**). Finally, when mapping the distribution of fPAR-CLIP sequence reads
374 across target RNAs little changes were observed in AGO target occupancy obtained from the
375 cytoplasmic fraction, with or without viral infection (**Fig 6A**). Contrary, the striking increase
376 in nuclear AGO transcript clusters, suggested that, once AGOs enter the nucleus, they expand
377 their binding preferences and interact with the pre-mRNA sequence. The predominant target
378 occupancy was on intronic sites, but also at 3'UTR and CDS regions within the nucleus (**Fig**
379 **6A**).

380 Next, we sought to investigate what targets the AGOs regulate upon viral infection. To
381 better visualize shifts in AGO-binding within the different cellular fractions, we plotted the
382 fPAR-CLIP signal, for all coding genes, in control (- virus) *vs* IAV-infected (+ virus) cells.
383 While dots on the axis indicate unique binders, a shift from the dashed line (x=y) denotes
384 enrichment in the number of AGOs binding to each transcript and/or the number of bound
385 transcripts. The resulting scatter plots highlighted no changes in the cytoplasmic environment
386 (**Fig 6B**) but a surge in AGO binding, within the nucleus, post-infection (**Fig 6C**). Genes
387 identified as having different distribution in the scatter plots, between IAV infected and non
388 infected samples, were defined as AGO2 targets. Taken together, the results demonstrate that,
389 upon IAV infection, not only is there an enrichment in nuclear AGO targets, but that more
390 AGOs are bound to each transcripts, upon viral infection.

391 Furthermore, to understand the effect of AGO-binding, we analyzed AGO binding
392 targets by cumulative distribution analysis, in relation to RNAseq experiment (**Sup Fig 6B**).
393 Here, a shift of the cumulative distribution function (CDF) curve to the left means that a higher
394 proportion of AGO targets are effectively suppressed, indicating that the RNAi machinery is
395 active and efficient. Consistent with the canonical function of cytoplasmic RNAi, we found
396 that AGO1-4 suppressed its best binding targets in the cytoplasm equally, regardless of IAV
397 infection (**Fig 6D,E**). On the contrary, in the nuclei of control cells, the differences in
398 expression fold change between AGO targets and non-targets are minor, as shown in the CDFs
399 and supported by the fact that AGOs are not present in the nucleus in steady state HEK293
400 cells (**Fig 6F**). However, we observed potent negative gene regulation of nuclear AGO fPAR-
401 CLIP targets, after IAV infection (**Fig 6G**).

402 Our previous data (**Fig 5**) suggested that AGO2 nuclear translocation correlated with a
403 decrease in type-I IFN pathway, which is crucial for antiviral responses. To test whether
404 nuclear AGOs had a direct effect on genes specifically involved in type-I IFN response, we
405 highlighted targets specifically involved in IFN-Is response [51] in the scatter plot and performed

406 CDF using those specific targets (**Fig 6H,I**). Indeed, 124 out of 131 genes were nuclear AGO
407 targets and were substantially downregulated by nuclear RNAi (**Fig 6H,I**).
408 To further gain insight into what genes AGO1-4 targets in the nucleus during viral
409 infection, we ranked the fPAR-CLIP targets of the AGOs (**Fig 6J, Sup Table 4**). Notably,
410 among the top AGO-bound transcripts in the nuclear fraction from viral-infected cells, three of
411 the top ten targets were in the 3'UTR and intronic regions of *LRP1B*, *TRIM71*, and *SOCS5* (**Fig**
412 **6J**). These molecules are well known for their significant roles in the immune response [11,52,53].
413 Of particular interest is *TRIM71* (also referred to as LIN41), renowned for its positive influence
414 on the IFNβ and ISRE responses but also directly inducing AGO2 and p53 degradation
415 processes [11,54,55]. Further elucidation from a STRING analysis revealed that AGO2
416 predominantly interacts with TRIM family proteins that plays a positive role in type-I
417 interferon pathway, especially with TRIM56, and TRIM71 (**Sup Fig 6F**). Our fPAR-CLIP
418 data, interpreted via the IGV software [56], clearly showed an enhanced AGO2 binding to
419 *TRIM71*, *LRP1B*, *SOCS5*, *IFNAR2* and *TRIM56* 3'UTR site following IAV infection,
420 compared to controls (**Fig 6K, Sup Fig 6G-J**). Substantiating this observation, post IAV-
421 infection, there was a significant decrease in TRIM71 and IFNAR2 protein levels (**Fig 6L, Sup**
422 **Fig 6K**). Finally, further examination of RNA-seq data showed downregulation of *TRIM71*
423 mRNA (log2FC -0.38), highlighting the dynamic response of host cellular machinery to viral
424 infection.
425 Our experimental data indicated that IAV infection promotes AGO2 nuclear
426 translocation, and the fPAR-CLIP results suggest two possible complimentary functions of
427 nuclear RNAi. 1) Direct silencing of genes involved in the type-I IFN pathways and, 2)
428 targeting of TRIM71 to block its direct effect on IFN response but also to prevent AGO2 and
429 p53 degradation. To experimentally test the latter, we overexpressed TRIM71 transiently in
430 IAV-infected HEK293; indeed, we observed a marked reduction in nuclear AGO2 levels (**Fig**
431 **6M**). This coincided with diminished p53 levels, aligning with the recognized role of TRIM71
432 as a p53 and AGO2 E3 ligase [11,54,55]. Consequently, there was an increase in *IFNB* (**Fig 6N**)
433 and other type-I IFN related genes mRNA levels (**Sup Fig 6L**), and a decrease in viral mRNA
434 (**Fig 6O**), attributable to the innate immune function of TRIM71 and decreased presence of
435 nuclear AGO2.
436 These insights suggest a nuanced viral strategy that involves AGO2-mediated gene
437 silencing combined with TRIM71 and IFNAR2 targeting. The culmination of these actions
438 dampens the type-I IFN pathway, allowing the virus to adeptly evade host immune defenses.

439 In summary, our integrated approach combining RNA sequencing and fPAR-CLIP
440 demonstrates that nuclear AGO2 is crucial for the virus to subvert host immune responses and
441 to ensure a successful infection.
442
443 **AGO2 targets TRIM71 through Let-7 miRNAs, upon IAV infection.**
444 AGO proteins exert their gene regulation by miRNAs. The miRNAs guide AGO to its target
445 RNA transcript and Watson-Crick basepairing allows for hybridization with the target, RISC
446 assembly and recruitment of effector complex for gene regulation [57]. Having determined that
447 TRIM71 is one of the top targets of AGO2 in the nucleus upon viral infection, we next wanted
448 to evalute which miRNAs are responsible for TRIM71 targeting. Using IGV software we
449 identified that AGO2 binds to two specific regions on the TRIM71 3'UTR (**Fig 6K**), which are
450 associated with the Let-7/98/4458/4500 and miR181abcd/4262 families (**Fig 7A,**). Given the
451 established role of Let-7 in cellular senescence, which is also caused by viral infection, we
452 focused our investigation on Let-7 [58,59]. To study the regulatory mechanism of Let-7 on AGO2
453 and its impact on cellular phenotype, we utilized LIN28, which is known to inhibit the
454 processing of Let-7 precursors, thus controlling the levels of mature Let-7 miRNAs [60]. First,
455 we overexpressed LIN28A and LIN28B in MCF7 cells and observed that LIN28A effectively
456 prevents the nuclear accumulation of AGO2 (**Sup Fig 7A**). We further tested the effect of
457 LIN28A overexpression on AGO2 localization in the context of PR8 infection in A549 and
458 HEK293 cells demonstrating that LIN28A does indeed reduces nuclear AGO2 accumulation
459 (**Fig 7B, Sup Fig 7B**). NS1 protein levels were also deacreased in viral infected and LIN28A
460 overexpressing cells, futher supporting that blocking nuclear AGO2 via Let-7 may reduce viral
461 infection (**Fig 7C**). To confirm a role for the miRNAs, we measured the levels of Let-7c, Let-
462 7f and Let-7g mature miRNA by qPCR and observed increased expression of Let-7c/f/g in
463 PR8-infected cells, in contast to control cells, which was promptly reduced by LIN28A
464 overexpression (**Fig 7D-F**). Together, these results provide compelling evidence that
465 modulating Let-7 levels, through LIN28A overexpression, impacts AGO2 dynamics and
466 potentially the cellular response to IAV infection.
467 To futher evaluate the link between nuclear AGO and gene silencing, we assessed the
468 global miRNA profiles bound to AGO proteins in the presence or absence of viral infection.
469 HEK293 cells were infected with PR8 virus, fractionated into cytoplasmic and nuclear
470 fractions, and AGO-specific targets were enriched by AGO1-4 pulled down using the T6B
471 peptide (**Sup Fig 7C**) before small RNA extraction and sequencing (**Sup Fig 7D**). Differential
472 expression analysis demonstrated significant changes in the nuclear fraction upon infection,

473 with significant upregulation of miRNAs, belonging to the Let-7 family, in the nuclear fraction
474 (**Fig 7G,H, Sup Table 5**). Similar changes were not observed in the cytoplasmic fraction, thus
475 confirming specific nuclear targeting of TRIM71 upon IAV infection (**Sup Fig 7E,F**). In order
476 to exclude a direct effect of miRNA on viral genes, we mapped sequencing reads to the IAV
477 genome and visualized targeting with IGV software. The tracks clearly showed no enrichment
478 over background upon infection thus discounting a direct role of nuclear or cytoplasmic AGO2
479 in miRNA-mediated silencing of viral genes (**Sup Fig 7G**). Overall, we demonstrate a critical
480 role for miRNAs of the Let-7 family, targeting TRIM71, in the AGO2-mediated nuclear
481 regulation of IAV infectivity.
482
483 **Nuclear p53-AGO2 axis is involved in regulation of innate immunity and IAV infectivity**
484 ***in vivo***
485 Our data demonstrates that AGO2 suppresses type-I IFN in the nucleus and that p53 is essential
486 to mediate AGO2 nuclear translocation. To confirm these mechanisms *in vivo*, we intranasally
487 (i.n.) administered IAV-PR8 to wild-type C57BL/6 mice. Lung tissues were harvested on days
488 1 and 3 post-infection (d.p.i.) (**Fig 8A**). As expected, mice infected with IAV exhibited
489 markedly elevated viral mRNA levels in lung tissues when compared to controls at 3 d.p.i. (**Fig**
490 **8B, Sup Fig 8A**). Next, we isolated single cells from both control and IAV-infected lung tissues
491 for biochemical fractionations assays. Healthy lung cells predominantly showed cytoplasmic
492 AGO2 distribution. In contrast, a notable nuclear accumulation of AGO2 was observed in
493 response to IAV infection (**Fig 8C**). To exclude that the positive AGO2 signal we observed in
494 the nuclear fraction was due to the influx of immune cells in the infected lungs [61], we carried
495 out a negative selection of $CD45^+$ immune cells. We found that AGO2 translocated to the
496 nucleus in both $CD45^+$ and $CD45^-$ cells, thus confirming that IAV infection induced AGO2
497 translocation in the epithelial and endothelial cells (**Sup Fig 8B**) and providing *in vivo* evidence
498 supporting IAV-mediated AGO2 nuclear translocation. To strengthen the role of NS1 *in vivo*,
499 we infected mice with PR8-$NS1_{1-124}$ mutant and collected lungs at 1 and 3 d.p.i. (**Sup Fig 8C**).
500 Mutant NS1 IAV infection did not induce AGO2 nuclear translocation (**Sup Fig 8D**) and,
501 accordingly, mice exhibited lower viral titers (**Sup Fig 8E,F**) and heightened *Ifnb* levels (**Sup**
502 **Fig 8G**).
503 To further explore the effects of AGO2 in the nucleus upon viral infection, we infected
504 *Tp53*$^{-/-}$ and C57BL/6 WT mice and harvested lungs at 3 d.p.i (**Fig 8D**). Supporting our *in vitro*
505 findings, AGO2 was not able to translocated to the nucleus in *Tp53*$^{-/-}$ mice (**Fig 8E**). Moreover,
506 in the *Tp53*$^{-/-}$ mice, we observed a significant reduction of viral mRNA levels and infectious

507 virus in the lungs (**Fig 8F,G**). TRIM71 was the second top target from our nuclear fPAR-CLIP
508 and a negative regulator of AGO2 and IFN levels. Interestingly, IAV-infected *Tp53*$^{-/-}$ mice
509 showed enhanced *Trim71* levels (**Fig 8H**), in line with all the results obtained *in vitro*.
510 Furthemore, *Tp53*$^{-/-}$ mice had increased *Ifnb* and *Ifnar2* mRNA levels (**Fig 8I,J**), again
511 supporting the *in vitro* mechanistic insights. Collectivly, our data indicate that absence of *Tp53*
512 *in vivo* significantly reduces viral infection.

513 To test whether pharmacological intervention could also result in beneficial antiviral
514 effects, we administered the FDA-approved ATO treatment known to monomerize p53 and
515 destabilize nuclear AGO2 (**Fig 3 and Sup Fig 3**). Mice received 0.15mg/kg of ATO for 4 days,
516 starting one day before infection, and lungs were harvested at 3 d.p.i. (**Sup Fig 8H**). Two
517 control groups received either daily vehicle injection or daily ATO injection, without infection.
518 The experimental groups received either daily vehicle injection + IAV i.n. infection or daily
519 ATO injection + IAV i.n. infection. At 3 d.p.i. single cells were isolated from lungs. It is
520 important to note that it was not possible to fully assess the efficacy of the ATO treatment *in*
521 *vivo*. Indeed, when using nuclear p53 levels, as a proxy of efficacy, ATO treatment was
522 successful in only ~50% of treated mice. However, whenever p53 was excluded from the
523 nucleus, we observed that also AGO2 was excluded regardless of IAV-infection, underscoring
524 the critical role p53 plays in nuclear AGO2 accumulation also *in vivo* (**Sup Fig 8I**). Therefore,
525 for our subsequent analysis we only considered mice where ATO treatment excluded p53 from
526 the nucleus. Indeed, also in this pharmacological model, we observed a trend towards reduced
527 viral mRNA levels and ~1-log reduction of infectious virus in the lungs of ATO-treated mice,
528 albeit not significant (**Sup Fig 8J,K**). Furthermore, *Trim71*, *Ifnb* and *Ifnar2* mRNA levels were
529 significantly enhanced in the ATO-treated mice (**Sup Fig 8L-N**).

530 Taken together, we unraveled a new layer of regulation of IAV infection and propose
531 that targeting either p53 or nuclear AGO2 might serve as a potential therapeutic avenue for
532 IAV modulation.

533

534 **DISCUSSION**

535 Unveiling mechanisms of viral resistance is crucial for designing effective new therapies to
536 alleviate disease. Here, by combining classical biochemical fractionation experiments with
537 fPAR-CLIP to identify the precise targets of nuclear AGO2 and *in vivo* mouse models we
538 discovered complex events leading to increased viral replication. We identified viral infection
539 as a potent trigger for nuclear AGO2 translocation, in complex with p53. In the nucleus, AGO2
540 suppresses innate immune genes thus favoring viral replication. By pinpointing the molecular

541 mechanisms involved, we could use the FDA approved drug arsenic trioxide to reverse AGO2
542 nuclear localization, increase innate immune response and lower viral infectivity.
543 In our study, we highlighted how certain viral components—specifically the large T
544 antigen from SV40 (a DNA virus) and NS1 from IAV (an RNA virus)—induce the nuclear
545 accumulation of both p53 and AGO2 (**Fig 2D,E**). This adds to the multiple proviral roles of
546 NS1 [30]. A limited number of previous reports already identified nuclear presence of AGO2
547 upon IAV infection [22,62], however both utilized cell lines (A549 and HEK293T) which are
548 already nuclear-AGO positive at steady state [25], thus complicating the interpretation of the
549 results. Herein, by using HEK293 cells, which are nuclear AGO negative at steady state, we
550 could better mimic what happens in mouse lungs. Indeed, also Wang et al described nuclear
551 accumulation of AGO2, mediated by NS1, and associated with increased virulence *in vivo*, but
552 did not provide any mechanistic explanation of the phenomenon [62]. In general, the translocation
553 of AGO2 from the cytoplasm to the nucleus is an intricate, dynamic process, elicited by a
554 spectrum of cellular stressors, including, but not limited to, cell confluence, DNA damage,
555 activation of oncogenes, and viral infections [20,62-65]. In our investigation, we observed nuclear
556 accumulation of AGO2 specifically in response to acute IAV infection (MOI ≥ 2). This
557 phenomenon was concomitant with the elevated expression of *GADD45B* (log2 fold change:
558 3.129), a key player in DNA damage repair and cellular senescence[66]. Fascinatingly, the
559 nuclear accumulation of p53 is also a characteristic feature of senescent cells [67]. Many *in vitro*
560 studies on innate antiviral immunity have been performed at low MOI, however in our work
561 we could observe only an effect starting from MOI 2. Interestingly, a detailed study analyzing
562 NS1 expression level and timing elegantly demonstrated that higher MOI is indeed essential
563 for potent and early NS1 expression [68]. Such expression was negatively correlated with
564 immune-related genes thus suggesting that the number of virions infecting a single cell
565 determined the antiviral response of that specific cell. Thus, we believe that early and potent
566 NS1 induction is a prerequisite for AGO2 nuclear translocation *in vitro* at the time points we
567 have analyzed. Possibly, lower MOI may also induce the same phenomena once NS1 is
568 expressed at higher level, which may take longer, but it was impossible to experimentally
569 assess due to technical limitations (**Sup Fig 1A**). Strongly supporting the physiological
570 relevance of our findings is the remarkable AGO2 nuclear translocation in lungs of IAV
571 infected mice (**Fig 8C**): *in vivo* cells are infected by single virions, initially, but thereafter
572 neighboring cells are infected at high MOI.
573 In addition, here we demonstrate that p53 is necessary to stabilize AGO2 in the
574 nucleus. We postulate that the tandem tryptophan-binding pockets within the PIWI domain of

575 AGO2 may serve as interaction sites with the flexible N-terminus of p53, characterized by
576 three tryptophan residues: Trp23, Trp53, and Trp91 (**Fig 3C**). While it was previously reported
577 that, in cancer, p53 and AGO2 interacted [69], here we further revealed the strong interaction
578 within the nucleus and complement it by demonstrating that the tetramerization of p53 may
579 enhance the stability of nuclear AGO2 (**Fig 3J**). p53 N-terminus, containing transactivation
580 domains and multiple phosphorylation sites, can also modulate DNA binding, potentially
581 influencing its interaction with proteins like MDM2, a p53 E3 ligase [70]. Further research is
582 needed to understand how AGO2-p53 interactions impact p53's DNA binding and protein
583 stability.

584 Here, we further elucidated the functional consequences of AGO2 nuclear
585 translocation. In general, RNAi function during viral infections is intricate and hotly debated:
586 it has been shown that RNAi can inhibit viral replication and augment the host immune
587 response, thus acting as an anti-viral factor, or promote viral replication and host immune
588 response evasion as a pro-viral factor [4,7,71,72]. While we have not studied in detail the potential
589 impact of direct RNAi against IAV, we have indirect evidence suggesting this does not play a
590 major role. Indeed, we did not detect neither enrichment of AGO targeting viral genes nor did
591 we detect any vial RNAs being loaded to AGO. Furthermore, by silencing p53 we did not affect
592 overall AGO2 levels, nevertheless we measured differences in viral mRNA, which was not
593 compatible with a direct antiviral role of RNAi. Notably, diminished levels of AGO2 mRNA
594 are reported in COVID-19 patients in comparison to healthy individuals [73]. Moreover, AGO4,
595 another effector in the RNAi/miRNA pathway, has illustrated antiviral properties in mammals
596 [74]. Together, the effects of AGO2 on viral infection can be governed by diverse variables such
597 as viral quantity, host cell type, expression level and subcellular localization of AGO2. Thus,
598 a nuanced understanding of the viral infection context is essential to decrypt the varied roles of
599 AGO2 in viral infections.

600 Our experimental data, combined with analysis of nuclear AGO targets by fPAR-CLIP
601 and miRNA-seq strongly indicated that nuclear AGO2 has a direct role in silencing the antiviral
602 interferon response in infected cells. This finding is consistent and mechanistically explains,
603 several sparse observations from previous studies: Backers *et al*. showed that in the absence of
604 small RNAs, *in vivo* RNA virus infection reached lower titers due to reduced repression of
605 antiviral genes; further, Seo *et al*, also postulated that inactivation of RISC would facilitate
606 antiviral response [6,7]. Yet another study identified AGO2 as negative regulator of IFNβ
607 signaling and another reported that p53 had direct impact on IFN-regulated genes, without

608 relying on its transcriptional activity [62,75]. Finally, it was also shown that Dicer-2 accumulation
609 had a negative effect on IFNβ signaling in human cells [76]. Altogether, the studies summarized
610 provided several pieces of information which we confirmed and expanded here in a
611 comprehensive mechanistical model, which includes a nuclear function of AGO2.
612 Furthermore, IAV NS1 causes global RNA PolII termination defects[77] and may promote
613 accumulation of aberrant transcripts, targeted by AGO2 in the nucleus. While this may play
614 some role, here we demonstrate that AGO2 is required for the effects observed.
615 In our quest to understand the molecular details by which IAV promotes AGO2:p53
616 accumulation within the nucleus, we utilized fPAR-CLIP to scrutinize the silencing targets of
617 nuclear AGO. Beside the IFN-pathways genes, discussed above, we underscored the pivotal
618 roles of nuclear E3 ligases, notably TRIM71 and MDM2. These ligases are instrumental in
619 determining the degradation pathways of AGO2 and p53, thereby influencing their nuclear
620 stability [54,78]. Our observations also underlined nuclear AGO targeted entities which are crucial
621 for p53 stability and its export to the cytosol, namely MDM2 and XPO1. Together, our results
622 indicate that the virus-induced presence of nuclear AGO2 appears to facilitate the aggregation
623 of AGO2:p53 in the nucleus and thus serving the dual role of stabilizing the complex and to
624 repress the antiviral immune response. TRIM71 was one of the top targets, also validated by
625 multiple miRNA targeting, and, beside its E3 ligase role, it has not been extensively studied;
626 neverthelessm it has been reported as immune enhancing protein, and, in a recent study, its
627 silencing resulted in increased SARS-CoV-2 viral titers [11,79]. Here we further validated
628 TRIM71 antiviral role and showed it to be associated with viral titer, IFN response and AGO2
629 stability both *in vitro* and *in vivo*.
630 The findings from our current work elucidate how the activation of p53, induced by
631 IAV, fosters the nuclear accumulation of AGO2, subsequently leading to the suppression of
632 innate immune genes, a scenario that can aggravate the clinical outcomes of IAV infection.
633 Such insights into the interplay between p53 activation and AGO2 translocation underscore the
634 potential of targeting p53-mediated AGO2 nuclear translocation as a viable therapeutic
635 strategy, as we have demonstrated using arsenic trioxide. Overall, our results could open new
636 avenues to slow down the progression and reduce the severity of viral infections.
637
638 **LIMITATIONS OF THE STUDY**
639 Here we demonstrated a link between nuclear AGO2:p53 translocation, the suppression of IFN
640 response and viral loads upon IAV infection. Although likely, we can not generalize our results

641 to other viral pathogens and/or other disease models, like cancers, which show increase
642 accumulation of nuclear AGO2. In addition, while we have individually silenced p53 and
643 AGO2 and shown that the majority of the effects we observe are due to AGO2, we cannot fully
644 exclude that stabilized nuclear p53 will impact transcription thus influencing some of our
645 results. Furthermore, broad changes in transcription upon *TP53* deletion may also contribute
646 to viral resistance in cell lines and mice and should be investigated in future studies.
647

648 **ACKNOWLEDGMENTS**

649 This work was funded by the European Research Council (ERC-StG, B-DOMINANCE, grant
650 no. 850638 to DA); the Swedish Research Council (grant no. 2021-01164, 2021-01165 to DA
651 and grant number 2019-01855 to AAS); the Knut and Alice Wallenberg Foundation (grant no
652 2021.0033 to DA and grant no PAR 2020/228 to AAS); the Swedish Society for Medical
653 Research (grant no S19-0019 to AAS) and the University of Gothenburg. J.O.W. is financially
654 supported by the Knut and Alice Wallenberg Foundation as part of the National Bioinformatics
655 Infrastructure Sweden at SciLifeLab. We are grateful to Dr. Marianne Farnebo (Karolinska
656 Institutet) for the generous contribution of TP53L expressing MCF7 cells. We would like to
657 thank the staff at the Experimental Biomedicine (EBM) core facility at the University of
658 Gothenburg for animal management. We thank SciLifeLab CRISPR Functional Genomics unit
659 at Karolinska Institutet for generating the TP53 KO HEK293 cells. The sequencing was
660 performed at the National Genomics Infrastructure (NGI).
661

662 **AUTHOR CONTRIBUTIONS**

663 H.-C.H. designed the experiments, performed the experiments, analyzed data, and wrote the
664 manuscript. D.A., D.G.A, and J.O.W. analyzed the NGS sequencing data. I.N. generated the
665 PAR-CLIP libraries, miRNAseq libraries and Let-7 qPCRs data. V.L. generated the PAR-CLIP
666 libraries and miRNAseq libraries. D.F.B. generated mutant NS1 virus. C.F. performed
667 immunofluorescent experiments. K.S., A.A.H.P., and C.W. performed animal experiments and
668 analyzed data. V.I.S. provided *Tp53*$^{-/-}$ mice, scientific input and feedback on the manuscript.
669 D.A. and A.A.S. supervised the entire project, designed the experiments, analyzed data, and
670 wrote the manuscript. All authors contributed to the manuscript
671

672 **DECLARATION OF INTEREST**

673 The authors declare no competing interests.
674

675 **METHODS**

676 **Mice and Ethical Statement**

677 All the experiments were conducted according to the protocols (Ethical permit numbers
678 1666/19, 38/23 and 2071/19) approved by regional animal ethics committee in Gothenburg.
679 Female, 8-12 weeks old C57BL/6 mice and *Tp53*$^{-/-}$ mice were purchased from Janvier, France.
680 They were housed in the specific pathogen-free animal facility of Experimental Biomedicine
681 Unit at the University of Gothenburg.

682

683 **Cell culture**

684 HEK293 (ATCC, CRL-1573), A549 (ATCC, CCL-185), HEK293T (ATCC, ACS-4500),
685 MCF7 (ATCC, HTB-22), MCF7 TP53L (kind gift from Dr. Marianne Farnebo, Karolinska
686 Institutet) and MDCK (ATCC, CCL-34) cell lines were cultured in Dulbecco's modified
687 Eagle's medium (DMEM) (Gibco, 11995065), supplemented with 10% fetal bovine serum
688 (FBS) (Gibco, 11573397) and 100 U/ml penicillin-streptomycin (Gibco, 11548876) in a
689 humidified incubator at 37°C and 5% CO2. The SK-N-BE(2) cell line was cultured in the same
690 medium, but with the addition of 1% non-essential amino acids (Gibco, 11140050). Vero cells
691 (kind gift from Dr. Kristina Nyström, University of Gothnburg) and MDCK cells, were grown
692 in DMEM (Gibco, 11594446) supplemented with 10% FBS (Gibco, 11550356) and 10 µg/ml
693 gentamicin (Gibco, 15710064) at 37°C. For the propagation of rescued virus in Vero cells,
694 DMEM was supplemented with 0.3% BSA (Sigma, A7906), 1 µg/ml TPCK-trypsin
695 (BioNordika, LS003740) and 10 µg/ml gentamicin. For the infection of Vero cells with the
696 rescued virus, DMEM supplemented with 1 mM HEPES (Gibco, 11560496), 5 µg/ml
697 gentamycin and 1 µg/ml TPCK-trypsin was used.

698

699 **TP53 knockout HEK293 by CRISPR**

700 Single guide (sg)RNAs were formed by duplexing crRNAs (5'
701 GCAGTCACAGCACATGACGG-3' and 5'- AATCAACCCACAGCTGCACA-3'; sg1 and
702 sg2 respectively; Alt-R® CRISPR-Cas9 crRNAs; IDT) with Alt-R™ CRISPR-Cas9 tracrRNA,
703 ATTO™ 647 (IDT) according to manufacturer's instructions. Equimolar mixtures of the two
704 sgRNAs were precomplexed with Cas9 protein (Alt-R® S.p. Cas9 Nuclease V3, IDT) into
705 ribonucleoproteins (RNPs). RNPs were introduced by electroporation into HEK293 cells using
706 the Neon system (ThermoFisher Scientific). Cells were expanded post-electroporation for
707 several days prior to genomic DNA extraction (QIAamp mini kit, QIAGEN).The frequency of

708 edited alleles was in first instance estimated by droplet digital PCR (ddPCR, QX200 System,
709 BioRad) in a dropoff assay, using a reference probe combined with a probe specific for the
710 wild type allele. After single-cell isolation, successful p53 knockout was confirmed by western
711 blot analysis, showing complete loss of p53 protein.
712
713 **Whole cell lysate and biochemical fractionation**
714 To extract whole cell lysates, the cells were first washed with cold 1xPBS and then lysed on
715 ice with RIPA lysis buffer (50 mM Tris-HCl, pH 7.6, 150 mM NaCl, 1 mM EDTA, 1% NP-
716 40, 1% sodium deoxycholate, 0.1% sodium dodecyl sulfate) supplemented with a protease
717 inhibitor cocktail (Merck Millipore, 04693132001). Samples were cleared with centrifugation
718 at 12 000 *g* for 20 minutes and the supernatant collected. Biochemical fractionation assay was
719 done as previously described [25,80]. Briefly, cell pellets were gently dissolved in a hypotonic
720 lysis buffer (10 mM Tris-HCl, pH 7.6, 10 mM NaCl, 3 mM $MgCl_2$, 0.3% NP-40, 10%
721 Glycerol), supplemented with a protease inhibitor cocktail, with gentle pipetting up and down
722 and collected with centrifugation for 2 minutes at 200 g. The supernatant was cleared with
723 centrifugation at 12 000 *g* for 20 minutes and the supernatant stored as the cytoplasmic fraction.
724 The remaining nuclear pellet was washed 3 times with the hypotonic lysis buffer and each time
725 collected by centrifugation for 2 minutes at 200 g. Each time the supernatant was discarded.
726 From the remaining pellet, the nuclear proteins were extracted using a nuclear lysis buffer (20
727 mM Tris-HCl, pH 7.6, 150 mM KCl, 3 mM $MgCl_2$, 0.3% NP-40, 10% Glycerol) supplemented
728 with protease inhibitor cocktail. The lysate was sonicated twice for 10 seconds each time at
729 60% amplitude (Sonics, VCX130). The nuclear fraction was cleared with centrifugation at
730 12 000 *g* for 20 minutes and the supernatant collected. Protein concentration was measured
731 using Bradford Reagent (B6916, Sigma Aldrich).
732
733 **Western blotting**
734 After protein extraction, as described above, 5-20 ug of protein were used for western blot
735 experiments. Protein samples were run on 4-12% Bis-Tris gels and transferred onto
736 Nitrocellulose membrane (Cytiva, 1060000). Proteins of interested were analyzed by
737 hybridization with their corresponding antibodies (see below) and visualized by
738 chemiluminescence using Thermo Scientific SuperSignal™ West Dura Extended Duration
739 Substrate (ThermoFisher, 34076).

FLAG (Merck, M8823)
HA (Sigma, H9658)

AGO1 (CST, 5053S)
AGO2 (Abcam, ab32381)
AGO2 11A9 for IF (Merck, MABE253)
AGO3 (CST, 5054)
β-Tubulin (Proteintech, 66240-1-Ig)
YB1 (Abcam, ab12148)
Histone H3 (CST, 44995)
p53 (Abcam, ab1101)
p53 (Santa cruz, sc-126)
p53 (ThermoFisher, MA5-11296)
GAPDH (Abcam, ab9485)
SV40 (Santa cruz, sc-147)
NS1 (ThermoFisher, PA5-32243)
TNRC6A (GW182) (Santa Cruz, sc56314)
mCherry (Santa cruz, sc-101529
Ubiquitin (Santa cruz, sc-8017).
TRIM71 (ThermoFisher, PA5-19281)
IFNAR2 (ThermoFisher, PA5-28303)
LIN28A (Santa cruz, sc-293120)
LIN28B (ThermoFisher, PA5-50609)
anti-rabbit IgG, HRP conjugate (Sigma, GENA934)
anti-mouse IgG, HRP conjugate (Sigma, GENA931)
anti-goat IgG, HRP conjugate (ThermoFisher, 10466033)
anti-sheep IgG, HRP conjugate (Merck, AP147P)
Anti-mouse Fc BP-HRP (Santa Cruz, sc525416)
Anti-rabbit IgG (Conformation Specific) (L27A9) mAb (HRP Conjugate) #5127

Plasmid transfection

Plasmids encoding the Influenza A virus components PB1, PB2, NP, M, HA, NA, NS1, PA and mCherry-NS1 were a kind gift from Dr. Ivan Kosik (NIH, USA). The SV40 Large T antigen and HA-TRIM71 were purchased from Addgene (plasmid # 136616 and #52717, respectively). LIN28A and LIN28B were also purchased from Addgene (plasmid # 51387 and #51373, respectively). 3 μg of plasmid was used for transient transfection using X-tremeGENE™ HP DNA Transfection Reagentreagent (Roche, 6366236001) following the manufacturer's instructions.

752 **NS1 mutagenesis**

753 The pDZ plasmid encoding NS1, kindly provided by Dr. Ivan Kosik from the NIH, USA, was
754 used as a template for site-directed deletion of its C-terminal regions spanning amino acids 81-
755 225 and 125-225. The resulting constructs encoded truncated NS1 proteins comprising amino
756 acids 1-80 and 1-124, respectively. These constructs were transiently transfected into HEK293
757 cells using the X-tremeGENE HP DNA Transfection Reagent (Roche, 6366236001) according
758 to the manufacturer's instructions. The expression of both full-length and truncated NS1
759 mutants was confirmed by western blotting using an anti-NS1 antibody (ThermoFisher, PA5-
760 32243).

761

762 **Viral infection in cells**

763 1 million HEK293 cells were seeded in 10 cm dishes. Cells were allowed to attach for 8 hrs
764 and were infected with PR8 with different MOI (0.1 to 10) for 16 hours in serum free media.
765 Cells were collected by trypsinization.

766

767 **Viral titer determination from infected lungs**

768 MDCK cells were seeded at 50,000 cells/well in 96-well plates. After overnight incubation,
769 cells were washed twice with PBS. Harvested lungs were placed in PBS at a constant w/v ratio.
770 Homogenized lungs were 10-fold diluted starting 1:10 in infection media (DMEM containing
771 0.1% BSA (fraction V; Roche), 10 mM HEPES (Corning), 500 µg/ml gentamicin (Gibco), and
772 1 µg/ml TPCK trypsin (Worthington) and incubated on MDCK cells. After 3 days cytopathic
773 effect was visualized after crystal violet staining and $TCID_{50}$ titer was calculated using the
774 Spearman and Karber method.

775

776 **Immunofluorescence staining and microscopy**

777 To perform immunofluorescence assay, HEK293 cells were either transfected with mCherry-
778 NS1 or infected with PR8-IAV, as described above, for 16 hours. Alternatively, HEK293 cells
779 were infected with mCherry-PR8 for 16 hours. Cells were washed with PBS and fixed with 4%
780 buffered formalin for 15 minutes at room temperature. Cells were then washed twice with PBS
781 and blocked with 5% BSA in PBS for 1 hour at room temperature. Finally, cells were incubated
782 with 1:200 AGO2 (Merck, MABE253) overnight. The next day cells were washed 3x with PBS
783 and probed with secondary antibodies: 1:2000 Alexa Fluor® 488 Goat Anti-Rat IgG
784 (Invitrogen, 10729174) or 1:1000 phalloidin (Invitrogen, 10643853) for 2 hours at room
785 temperature. To visualize the cell nuclei, 4',6-diamidino-2-phenylindole (DAPI; Invitrogen,

786 D3571) was added for 5 minutes in the dark. Slides were mounted using 10 µl Prolong Diamont
787 (Invitrogen, 15372192). Confocal images were taken on a Zeiss LSM780 and the images were
788 analyzed using ImageJ® software and Affinity Designer®.
789
790 **Doxorubicin treatment**
791 Doxorubicin (Biotechne (Tocris), 2252) was dissolved in dimethyl sulfoxide (DMSO) to
792 prepare a 1 mM stock solution. The stock solutions were stored at -20°C and diluted in the
793 culture medium to 1 µM final concentrations. Cells were incubated with doxorubicin for 24
794 hours.
795
796 **Immunoprecipitation assays and AGO protein affinity purification with T6B peptide**
797 Immunoprecipitation was carried out in 1-3 mg of protein lysate and 2 µg of anti-AGO2, anti-
798 IgG, or anti-p53 antibodies. For purification of AGO1-4, 400 µg Flag-tagged T6B peptide was
799 used [50]. Dynabead Protein G beads (10004D, ThermoFisher) or anti-Flag M2 beads (M8823,
800 Millipore) were conjugated with either antibodies or T6B peptide, respectively, for 4 h, washed
801 and incubated with protein lysates. Next, beads were washed three times with RIPA buffer and
802 bound proteins were eluted at 95°C for 5 min in 3× SDS Laemmli buffer and assessed by
803 western blot. The pull-down efficiency was confirmed by western blot.
804
805 **p53 mutagenesis**
806 The plasmid encoding amino acids 1-393 of the p53 protein with a FLAG tag at the C-terminus
807 (Addgene plasmid #10838) was used as a template for site-directed mutagenesis to delete the
808 N-terminal regions spanning amino acids 1-31, 1-62, or 1-93. The resulting PCR products were
809 cloned into the pcDNA3.1 expression vector (Invitrogen, v79020). The final constructs
810 encoded truncated p53 proteins with a FLAG tag starting at amino acids 32, 63, or 94,
811 respectively. The pcDNA3 constructs were used for transient transfection in HEK293 cells
812 using an X-tremeGENE HP DNA Transfection Reagent (Roche, 6366236001) according to the
813 manufacturer's instructions. The expression of the full-length and truncated p53 proteins were
814 verified by western blotting using an anti-FLAG antibody (Merck, M8823).
815
816 **Arsenic trioxide (ATO) treatment**
817 Arsenic trioxide (Merck, 202673-5G) was dissolved to 100 mg/ml stock solution in NAOH
818 which was further diluted in DMEM to 1 mg/ml. The stock solutions were stored at -20°C and

819 diluted in the culture medium to 0.01, 0.1 or 0.5 μg/ml concentrations before use. Cells were
820 incubated with ATO for 24 hours.
821
822 **siRNA Gene Silencing of AGO2 and TP53**
823 Small interfering RNA (siRNA) targeting human *AGO2* (siRNA ID: s109013 and ID s25931),
824 *TP53* (siRNA ID s607), and scramble control siRNAs (siRNA ID: 4390843) were purchased
825 from ThermoFisher Scientific. Human A549, HEK293T, MCF7, or SK-N-BE(2) cells were
826 transfected with the siRNAs using Lipofectamine RNAiMAX Transfection Reagent
827 (ThermoFisher Scientific, #13778030) according to the manufacturer's instructions. The cells
828 were harvested 48 hours after siRNA transfection to evaluate AGO2 or p53 knock-down
829 efficiency by quantitative RT-qPCR and protein level by western blotting.
830
831 **MG132 treatment and ubiquitination assay**
832 MG132 (ThermoFisher, 15465519) were dissolved in dimethyl sulfoxide (DMSO) to prepare
833 a 10 mM stock solution. The stock solutions were stored at -20°C and diluted in the culture
834 medium to 40 μM concentrations before use. Cells were treated with MG132 or DMSO only
835 for 4 hours. Following the treatment, cells were lysed and/or fractionated and assessed by
836 western blotting.
837
838 **Protein-protein docking and structure modelling**
839 To predict the interaction between PIWI domain of AGO2 (570-859 amino acid) with the T6B
840 peptide from TCRC6B (599-683 amino acid) or N-terminal of p53 (1-94), we performed
841 molecular docking by using the HDOCK server [42]. This server uses the hybrid algorithm of
842 template bases modeling and ab initio free docking and provides the top ten complex models
843 with the highest scores. Among the top 10 models for both complexes, the first models with
844 the lowest docking scores and highest confidence scores. Specifically, the first model of the
845 AGO2 with T6B peptides from TNRC6B complex has a docking score of −308.41 and a
846 confidence score of 0.9596, while the first model of AGO2 with N-terminal of p53 complex
847 has a docking score of −268.89 and a confidence score of 0.9151. To model the structures of
848 p53 (AF-P04637-F1), we downloaded their atomic coordinates from the AlphaFold2 database
849 [81]. We used the PyMOL Molecular Graphics System, Version 2.3.4 (Schrödinger, LLC,
850 https://pymol.org/2/) to visualize and modify the structure figures.
851

852 **Real-time quantitative PCR (RT-qPCR)**

853 To analyze gene expression levels, real-time quantitative PCR (RT-qPCR) was performed on
854 the following cell lines: HEK293, TP53 KO HEK293, HEK293T, A549, MCF7 and MCF7
855 TP53L. Total RNA was isolated from each cell line using the Quick-RNA Miniprep Kit
856 (ZYMO Research, R1055) following the manufacturer's instructions. To generate cDNA, 1 µg
857 of total RNA was used in a reverse transcription reaction with the iScript cDNA Synthesis kit
858 (Bio-Rad, 1708891) according to the manufacturer's instructions. The RT-qPCR reactions were
859 performed in a 10 µL mixture, consisting of 1x iQ™ SYBR® Green supermix (Bio-Rad,
860 1708880), 0.5 µmol/L of each primer, and 10 ng of cDNA template. The RT-qPCR result was
861 acquired by CFX Connect Real-Time PCR Detection System (Bio-Rad) using the following
862 primers:

AGO2 forward	5'- CAAGTCGGACAGGAGCAGAAAC-3'
AGO2 reverse	5'- GACCTAGCAGTCGCTCTGATCA-3'
P53 forward	5'- CCTCAGCATCTTATCCGAGTGG-3'
P53 reverse	5'- TGGATGGTGGTACAGTCAGAGC-3'
IFNA forward	5'- AGAAGGCTCCAGCCATCTCTGT-3'
IFNA reverse	5'- TGCTGGTAGAGTTCGGTGCAGA-3'
IFNB forward	5'- CTTGGATTCCTACAAAGAAGCAGC-3'
IFNB reverse	5'- TCCTCCTTCTGGAACTGCTGCA-3'
TRIM71 forward	5'- CGAGGCATAAGAAAGCCCTGGA-3'
TRIM71 reverse	5'- GCTTGTTGAGGTTTTGCCGCAG-3'
IFNAR1 forward	5'- CGCCTGTGATCCAGGATTATCC-3'
IFNAR1 reverse	5'- TGGTGTGTGCTCTGGCTTTCAC-3'
IFNAR2 forward	5'- ACCGTCCTAGAAGGATTCAGCG-3'
IFNAR2 reverse	5'- CCAACAATCTCAAACTCTGGTGG-3'
Mouse ifna2 forward	5'- GAGCCTAGAGACTATCACACCG-3'
Mouse ifna2 reverse	5'- TACCAGAGGGTGTAGTTAGCGG-3'
Mouse ifnb1 forward	5'- GCCTTTGCCATCCAAGAGATGC-3'
Mouse ifnb1 reverse	5'- ACACTGTCTGCTGGTGGAGTTC-3'
Mouse trim71 forward	5'- AGATGAAGGCGAAGGTGGTCCA-3'
Mouse trim71 reverse	5'- GCAGGAACAGAGACTTCGCCTT-3'
Mouse b-actin forward	5'- CATCCGTAAAGACCTCTATGCCAAC-3'
Mouse b-actin reverse	5'- CAAAGAAAGGGTGTAAAACGCAGC-3'
HA forward	5'-AAGGCAAACCTACTGGTCCTGTT-3'
HA reverse	5'- AATTGTTCGCATGGTAGCCTATAC-3'
NA forward	5'- AGGCACCAAACGGTCTTACG-3'
NA reverse	5'- TTCCGACGGATGCTCTGATT-3'
NP forward	5'- AGGCACCAAACGGTCTTACG-3'
NP reverse	5'- TTCCGACGGATGCTCTGATT -3'
NS1 forward	5'- AAATCAGAAAATAACAACCATTGGA-3'
NS1 reverse	5'- ATTCCCTATTTGCAATATTAGGCT-3'
ISG15 forward	5'- CTCTGAGCATCCTGGTGAGGAA-3'
ISG15 reverse	5'- AAGGTCAGCCAGAACAGGTCGT-3'

ISG20 forward	5'- ACACGTCCACTGACAGGCTGTT-3'
ISG20 reverse	5'- ATCTTCCACCGAGCTGTGTCCA-3'
OAS1 forward	5'- AGGAAAGGTGCTTCCGAGGTAG-3'
OAS1 reverse	5'- GGACTGAGGAAGACAACCAGGT-3'
OAS3 forward	5'- CCTGATTCTGCTGGTGAAGCAC-3'
OAS3 reverse	5'- TCCCAGGCAAAGATGGTGAGGA-3'
PARP12 forward	5'- CTCTGTCACCAAACCTCCACAC-3'
PARP12 reverse	5'- GCTACTGCTGACAGTGGTCACA-3'
TRIM25 forward	5'- AAAGCCACCAGCTCACATCCGA-3'
TRIM25 reverse	5'- GCGGTGTTGTAGTCCAGGATGA-3'

Flow cytometry

HEK293 and TP53 KO HEK293, as well as MCF7 and MCF7 TP53L cells were infected with PR8-NS1-mCherry at multiplicity of infection (MOI) 10 for 16 hours. Cells were collected by trypsinization and resuspended in FACS buffer. Cells were acquired using BD LSR II flow cytometer (BD Bioscience) to measure the expression of mCherry in HEK293 and TP53 KO HEK293, as well as MCF7 and MCF7 TP53L cells. Data analysis was performed using FlowJo V10 software (Treestar).

Luciferase assay

Cells were seeded 200,000 cells in 12 well dishes. The next day, the cells were transfected with ISRE reporter plasmid (a gift from Dr. Chia-Wei. Li, Academia Sinica, Taiwan) or with the internal control SV40 renilla plasmid (Promega) for 24 hours and subsequently infected with PR8 at MOI 10 for an additional 16 hours. Cells were then collected for luciferase assay using the Dual-Luciferase Reporter assay (Promega, E1910), following manufacturers´ instructions. Plates were read using CLARIOstar Plate Reader (BMG Labtech).

RNA-sequencing

Total RNA was extracted from HEK293 with or without PR8 infection (MOI:10) for 16 hours, using the Quick-RNA Miniprep Kit (ZYMO Research) following the manufacturer's protocol. the concentration and quality of the RNA was analyzed using Agilent 2200 TapeStation System. RNA samples with RNA Integrity Number higher than 8 were sent to SNP&SEQ Technology Platform (NGI Uppsala, Sweden). Libraries were prepared from 300 ng RNA using the Illumina Stranded Total RNA library preparation kit, including Ribo-Zero Plus treatment (20040525/20040529, Illumina Inc.) according to manufacturer's instructions. For indexing Unique Dual Indexes (20040553/20040554, Illumina Inc.) were used. Sequencing was carried out with NovaSeq 6000 system using paired-end 150 bp read length, S4 flowcell

890 and v1.5 sequencing chemistry. As a control sequencing library for the phage PhiX was
891 included and a 1% spike-in in the sequencing run. RNAseq data were preprocessed using the
892 RNAseq nf-core pipeline [82]. Differential expression analysis was done using DEseq2 [83], on
893 genes with at least 10 reads in at least 3 samples. Genes with FDR adjusted p-value < 0.01 and
894 absolute log2 fold change > 0.5 were considered differentially expressed. Hypergeometric
895 tests, implemented in TopGO, were used to look for enriched Gene Ontology annotation among
896 the differentially expressed genes. The fraction of reads mapping to introns and other genomic
897 regions was calculated using ReSQC [84].
898
899 **Fluorescent PhotoActivatable Ribonucleoside-enhanced CrossLinking and**
900 **ImmunoPrecipitation (fPAR-CLIP)**
901 AGO fPAR-CLIP was carried out by isolating the proteins using the T6B peptide as mentioned
902 above. fPAR-CLIP library preparation, sequencing and initial data processing was performed
903 as described in [25,49] with minor modifications. Briefly, to obtain AGO proteins RNA footprints,
904 unprotected RNA was digested on beads with 1 U RNase T1 (EN0541, ThermoFisher) for 15
905 min at RT. Next, the beads were washed three times with RIPA buffer and three times with
906 dephosphorylation buffer (50 mM Tris–HCl, pH 7.5, 100 mM NaCl, 10 mM $MgCl_2$). After
907 washing, the protein-bound RNA was dephosphorylated with Quick CIP (M0525S, New
908 England Biolabs) for 10 min in 37°C. Post dephosphorylation the beads were washed three
909 times with dephosphorylation buffer and three times with PNK/ligation buffer (50 mM Tris-
910 HCl, pH 7.5, 10 mM $MgCl_2$). Following, 0,5 µM fluorescently tagged 3' adapter
911 (MultiplexDX) were ligated with T4 Rnl2(1–249)K227Q (M0351, New England Biolabs)
912 overnight at 4°C and washed three times with PNK/ligation buffer. Next, RNA footprints were
913 phosphorylated using T4 PNK (NEB, M0201S) for 30 min in 37°C and washed three times in
914 RIPA buffer. To release the proteins the beads were incubated at 95°C for 5 min in 3× SDS
915 Laemmli buffer. Next, the eluates were separated on a 4-12% SDS/PAGE gels
916 (NW04122BOX, Invitrogen) and AGO:RNA complexes visualized on the IR 680 channel
917 (Chemidoc MP system, Bio-Rad). Subsequently, appropriate AGO:RNA bands were excised
918 from the gel and protein digested with Proteinase K (RPROTK-RO, Sigma Aldrich) and
919 released RNA isolated via phenol:chloroform phase separation. Following, 5' adapter ligation
920 (MultiplexDX) was performed on the purified RNA samples with 0,5 µM of the adapter and
921 Rnl1 T4 RNA ligase (ThermoFisher, EL0021) for 1 h at 37°C. Next, the RNA was reverse
922 transcribed using SuperScript IV Reverse Transcriptase (ThermoFisher, 18090010) according
923 to manufacturer's instructions. The libraries were amplified in a series of PCR reactions

924 performed using Platinum Taq DNA polymerase (ThermoFisher, 10966034) and size selected
925 with 3% Pippin Prep (Sage Science, CSD3010). Sequencing of the libraries was carried out on
926 Illumina NovaSeq 6000 platform. For data processing Bcl2fastq (v2.20.0), Cutadapt (cutadapt
927 1.15 with Python 3.6.4) [85], PARpipe (https://github.com/ohlerlab/PARpipe) and Paralyzer [86]
928 were used. The 3' and 5' adaptor sequences and sequencing primers used in the study are listed
929 below. For each target gene, the normalized PAR-CLIP signal was calculated as nr reads with
930 T->C conversions / (total number of PAR-CLIP reads * average TPM for target gene * 1e-6)

Oligo name	Sequence
3' adapter	5'-rAppNNTGACTGTGGAATTCTCGGGT(fl)GCCAAGG-(fl) (MDX-O-226-29.51-2xAF660, Multiplexdx)
5' adapter	5'(aminolinker)GTTCAGAGTTCTACAGTCCGACGATCrNrNrNrN (MDX-O-264, Multiplexdx)
RT Primer	GCCTTGGCACCCGAGAATTCCA
5' short PCR primer	CTTCAGAGTTCTACAGTCCGACGA
5' long PCR primer	AATGATACGGCGACCACCGAGATCTACACGTTCAGAGTTCTACAGTCCGA
HEK293 Cont C1 3' Index primer RPI29-C5	CAAGCAGAAGACGGCATACGAGATATTCCTCCGTGACTGGAGTTCCTTGGCACCCGAGAATTCCA
HEK293 Cont C2 3' Index primer RPI30-C6	CAAGCAGAAGACGGCATACGAGATGTGTTCCTGTGACTGGAGTTCCTTGGCACCCGAGAATTCCA
HEK293 Cont N1 3' Index primer RPI23-B11	CAAGCAGAAGACGGCATACGAGATAACCTTGGGTGACTGGAGTTCCTTGGCACCCGAGAATTCCA
HEK293 Cont N2 3' Index primer RPI24-B12	CAAGCAGAAGACGGCATACGAGATATTGCGTGGTGACTGGAGTTCCTTGGCACCCGAGAATTCCA
HEK293 Virus C1 3' Index primer RPI31-C7	CAAGCAGAAGACGGCATACGAGATAAGCACTGGTGACTGGAGTTCCTTGGCACCCGAGAATTCCA
HEK293 Virus C2 3' Index primer RPI32-C8	CAAGCAGAAGACGGCATACGAGATCTAGCAAGGTGACTGGAGTTCCTTGGCACCCGAGAATTCCA
HEK293 Virus N1 3' Index primer RPI27-C3	CAAGCAGAAGACGGCATACGAGATGTACTCTCGTGACTGGAGTTCCTTGGCACCCGAGAATTCCA
HEK293 Virus N2 3' Index primer RPI28-C4	CAAGCAGAAGACGGCATACGAGATGTAACGACGTGACTGGAGTTCCTTGGCACCCGAGAATTCCA

931

932 **miRNA sequencing**

933 AGO proteins were immunoprecipitated from 200 mg of protein using Flag-tagged T6B
934 peptide. AGO-bound RNA was recovered from the beads using TRIzol reagent (Invitrogen,
935 15596026) according to the manufactures instructions and small RNA libraries were produced
936 as previously described [49], with minor modifications. Briefly, 3' adapters with 5'-adenylated
937 RNA adapter (see 3' adapters in table below) were ligated to the recovered small RNAs using

938 Rnl2(1-249)K227Q RNA ligase (New England Biolabs, M0351) at 4°C overnight with
939 constant shaking. Ligated RNA was pooled within conditions and purified using oligo clean
940 and concentrate kit (ZYMO Research, D4060). Next, the RNA was subjected to 5' adapter
941 ligation with a 5' chimeric DNA-RNA adapter (5'aminolinker-
942 GTTCAGAGTTCTACAGTCCGACGATCrNrNrNrN) using RNA ligase (ThermoFisher
943 Scientific, EL0021) at 37°C for 1 hour. Next, the RNA was purified using oligo clean and
944 concentrate kit and reverse transcribed using SuperScript® IV (ThermoFisher Scientific,
945 18090010) using RT primer (GCCTTGGCACCCGAGAATTCCA). The cDNA was amplified
946 using Platinum Taq DNA Polymerase (ThermoFisher Scientific, 10966034), according to the
947 manufacturer's instructions using 5'-medium PCR primer
948 (CTCTACACGTTCAGAGTTCTACAGTCC) and 3' medium PCR primer
949 (CCTGGAGTTCCTTGGCACCCGAGAATT) for 6 cycles. Then the PCR product was
950 purified using the oligo clean and concentrate kit, eluted with 32 µl of nuclease free water, and
951 size selected (74-88 bp) using 3% agarose Pippin Prep (Sage Science, CSD3010). Following
952 size selection, a second round of (X cycle) PCR was performed using the same polymerase, a
953 5'- long PCR primer:
954 AATGATACGGCGACCACCGAGATCTACACGTTCAGAGTTCTACAGTCCGA, and 3'
955 indexed primer (see 3' index primers in table below). Libraries were sequenced on an Illumina
956 NovaSeq6000. Bcl files were converted to fastq files using bcl2fastq. Adapters were trimmed
957 using cutadapt v 2.4. and reads were mapped to the human miRNAs using bowtie [87].

Sample	**Illumina Index primer**	**3' adapter**
Ctrl C1	CAAGCAGAAGACGGCATACGAG ATAGGTCACTGTGACTGGAGTT CCTTGGCACCCGAGAATTCCA	5'-rAppNNTCTGTGTGGAATTCTCGGGTGCCAAGG-L
Ctrl C2		5'-rAppNNCAGCATTGGAATTCTCGGGTGCCAAGG-L
Ctrl C3		5'-rAppNNATAGTATGGAATTCTCGGGTGCCAAGG-L
Ctrl C4		5'-rAppNNTCATAGTGGAATTCTCGGGTGCCAAGG-L
Ctrl N1	CAAGCAGAAGACGGCATACGAG ATGAATCCGAGTGACTGGAGTT CCTTGGCACCCGAGAATTCCA	5'-rAppNNTCTGTGTGGAATTCTCGGGTGCCAAGG-L
Ctrl N2		5'-rAppNNCAGCATTGGAATTCTCGGGTGCCAAGG-L
Ctrl N3		5'-rAppNNATAGTATGGAATTCTCGGGTGCCAAGG-L
Ctrl N4		5'-rAppNNTCATAGTGGAATTCTCGGGTGCCAAGG-L
PR8 C1	CAAGCAGAAGACGGCATACGAG ATCATGAGGAGTGACTGGAGTT CCTTGGCACCCGAGAATTCCA	5'-rAppNNTCTGTGTGGAATTCTCGGGTGCCAAGG-L
PR8 C2		5'-rAppNNCAGCATTGGAATTCTCGGGTGCCAAGG-L
PR8 C3		5'-rAppNNATAGTATGGAATTCTCGGGTGCCAAGG-L
PR8 C4		5'-rAppNNTCATAGTGGAATTCTCGGGTGCCAAGG-L
PR8 N1	CAAGCAGAAGACGGCATACGAG ATTGACTGACGTGACTGGAGTT CCTTGGCACCCGAGAATTCCA	5'-rAppNNTCTGTGTGGAATTCTCGGGTGCCAAGG-L
PR8 N2		5'-rAppNNCAGCATTGGAATTCTCGGGTGCCAAGG-L

PR8 N3		5'-rAppNNATAGTATGGAATTCTCGGGTGCCAAGG-L
PR8 N4		5'-rAppNNTCATAGTGGAATTCTCGGGTGCCAAGG-L

958

959 **miRNA RT-qPCR**

960 Reverse transcription of miRNA species was performed with miRCURY LNA™ Universal RT
961 microRNA PCR (Qiagen, 339340). 500 ng total RNA was used per reaction. For miRNA RT-
962 qPCR experiments miRCURY LNA SYBR Green PCR Kit (Qiagen, 339345,) was used. For
963 qPCR reactions, the cDNA was diluted 60 times and miRNA-16-5p was used as the reference
964 gene. Primers for miRNA-16-5p (YP00205702), let-7c-5p (YP00204767), let-7f-5p
965 (YP00204359) and let-7g-5p (YP00204565) were provided by Qiagen. All RT-qPCR
966 experiments were performed in triplicate at least three times, and relative let-7 family miRNAs
967 expression was calculated using the ΔΔCq method [88].

968

969 **Virus Rescue**

970 Virus containing mutant NS1 genes were rescued as previously described [89]. Briefly, the day
971 before transfection, HEK293T cells were seeded at 500,000 per well in 6-well plates. The next
972 day, cells were transfected with 1 µg of each plasmid of the eight gene segments of IAV using
973 Lipofectamine 2000 transfection reagent (Invitrogen, 11668-019) in Opti-MEM reduced serum
974 medium (Gibco, 31985-062), according to manufacturer's instructions. The plates were
975 incubated for 24-, 36-, and 48- hours, and supernatants collected to be used for inoculation of
976 7 days embryonated chicken eggs and Vero cells for propagation. The presence of the mutant
977 NS1 gene segment after transfection was verified using PCR amplification: Forward primer
978 full length NS1: TGGATCCAAACACTGTGTCAAGC, Reverse primer full length NS1:
979 ACCTAATTGTTCCCGCCATTTCTC), Reverse primer mutant NS1 1-80:
980 TTTCAGAATCCGCTCCACTATCTGC, Reverse primer mutant NS1 1-124:
981 GTCCATTCTGATACAAAGAGGGCCT. Rescue was confirmed by hemagglutination assay.

982

983 **Rescued virus $TCID_{50}$ determination**

984 After rescuing the virus, viral titre was assessed using ELISA assay. The day before the assay,
985 96-well flat-bottomed plates were seeded with 100 µl of 100,000 Vero cells per well and
986 incubated at 37°C overnight to allow for the cells to reach full confluency. Next day, the cells
987 were washed twice with PBS and 180 ml of infection media was added per well. The virus was
988 then added to column 1, at 1:10 dilution in quadruplicate, and ten-fold serially diluted across
989 the plate with the last column as the cells only control. The plates were incubated at 37°C for

990 20 hours. After incubation, the cells were washed once with PBS and fixed with 50 µl/well ice-
991 cold methanol at 4ºC for 10 minutes. Following the fixation, the cells were again washed with
992 PBS then 100 µl/well of the primary ascites anti-NP HB65 antibody (kind gift from Dr.
993 Jonathan Yewdell, NIH), at 1:10000 dilution, was added and allowed to incubate for 2 hours
994 at room temperature. Plates were washed thrice with PBS + 0.05% Tween followed by the
995 addition of 50 µl/well of the secondary rat anti-mouse kappa HRP antibody (Southern Biotech,
996 1170-05, at 1:1000 dilution, and incubated for 1 hour at room temperature. After a final three
997 times wash with PBS-T, the plates were developed by adding 50 µl/well of TMB
998 (ThermoFisher, 34029) and incubated in the dark for 5 minutes at room temperature. The
999 reaction was stopped with the addition of 25 µl/well of 2M H_2SO_4 and the absorbance were
1000 read with TECAN Sunrise absorbance microplate reader (16039400) at 450nm. Analysis of the
1001 results was carried out using the Reed and Muench infectivity calculator.
1002
1003 **Virus infection in mice**
1004 The H1N1 strain of influenza A/PR8 (Puerto Rico/8/34) was propagated in the allantoic
1005 cavities of SPF embryonated chicken eggs for 48-72 hours at 37°C. The resulting allantoic
1006 fluids were collected, aliquoted, and stored at -80°C until use. Virus titers were assessed by
1007 $TCID_{50}$ assay on MDCK cells as previously reported [90]. To infect the mice, they were
1008 anaesthetized with isoflurane, and intranasally inoculated with 2000 TCID50 PR8 in 25 µl
1009 sterile PBS/0.1%BSA. Control mice received the same volume of PBS intranasally as a mock
1010 infection. After three days of infection, lung tissue samples were collected to isolate single
1011 cells using the Lung Dissociation Kit (130-095-927, Miltenyl Biotec, Bergisch Gladbach,
1012 Germany) following the manufacturer's protocol. RNA and protein were extracted from the
1013 isolated single cells to determine viral mRNA and AGO2 distribution. Specifically, the RNA
1014 was extracted using a Quick-RNA Miniprep Kit (ZYMO Research) following the
1015 manufacturer's protocol, and the protein was extracted using biochemical fractionation method
1016 described above. For ATO treatment, mice were injected intraperitoneally with a daily dose of
1017 0.15mg/kg ATO in PBS in a volume of 100 µl for 4 days.
1018
1019 **Data availability**
1020 The raw RNA-Seq and PAR-CLIP data described in this paper are accessible through the GEO
1021 database (https://www.ncbi.nlm.nih.gov/geo/) under accession no. xxx and xxx. miRNAseq

1022 data are accessible through the GEO database (https://www.ncbi.nlm.nih.gov/geo/) under
1023 accession no. xxx
1024
1025 **Statistical analysis**
1026 The data from three individual experiments waere assessed by unpaired t-test or Mann-
1027 Whithney U-test (GraphPad Prism Software Inc, San Diego, CA, USA) and presented as mean
1028 ± SD (standard deviation). A p-value < 0.05 was considered statistically significant.
1029 Cumulative distribution was analyzed using Kolmogorov-Smirnov Test using the R package
1030 stats.
1031
1032 **References**

1033 1. Wilson, R.C. & Doudna, J.A. Molecular mechanisms of RNA interference. *Annu Rev*
1034 *Biophys* **42**, 217-39 (2013).
1035 2. van Rij, R.P. et al. The RNA silencing endonuclease Argonaute 2 mediates specific
1036 antiviral immunity in Drosophila melanogaster. *Genes Dev* **20**, 2985-95 (2006).
1037 3. Li, W.X. et al. Interferon antagonist proteins of influenza and vaccinia viruses are
1038 suppressors of RNA silencing. *Proc Natl Acad Sci U S A* **101**, 1350-5 (2004).
1039 4. Li, Y. et al. Induction and suppression of antiviral RNA interference by influenza A
1040 virus in mammalian cells. *Nat Microbiol* **2**, 16250 (2016).
1041 5. Lopez-Orozco, J. et al. The RNA Interference Effector Protein Argonaute 2 Functions
1042 as a Restriction Factor Against SARS-CoV-2. *J Mol Biol*, 168170 (2023).
1043 6. Backes, S. et al. The Mammalian response to virus infection is independent of small
1044 RNA silencing. *Cell Rep* **8**, 114-25 (2014).
1045 7. Seo, G.J. et al. Reciprocal inhibition between intracellular antiviral signaling and the
1046 RNAi machinery in mammalian cells. *Cell Host Microbe* **14**, 435-45 (2013).
1047 8. Aguado, L.C. et al. microRNA Function Is Limited to Cytokine Control in the Acute
1048 Response to Virus Infection. *Cell Host Microbe* **18**, 714-22 (2015).
1049 9. Diamond, M.S. & Kanneganti, T.D. Innate immunity: the first line of defense against
1050 SARS-CoV-2. *Nat Immunol* **23**, 165-176 (2022).
1051 10. Schneider, W.M., Chevillotte, M.D. & Rice, C.M. Interferon-stimulated genes: a
1052 complex web of host defenses. *Annu Rev Immunol* **32**, 513-45 (2014).
1053 11. Versteeg, G.A. et al. The E3-ligase TRIM family of proteins regulates signaling
1054 pathways triggered by innate immune pattern-recognition receptors. *Immunity* **38**, 384-
1055 98 (2013).
1056 12. Wang, X. et al. Influenza A virus NS1 protein prevents activation of NF-kappaB and
1057 induction of alpha/beta interferon. *J Virol* **74**, 11566-73 (2000).
1058 13. Evseev, D. & Magor, K.E. Molecular Evolution of the Influenza A Virus Non-structural
1059 Protein 1 in Interspecies Transmission and Adaptation. *Front Microbiol* **12**, 693204
1060 (2021).
1061 14. Hale, B.G., Albrecht, R.A. & García-Sastre, A. Innate immune evasion strategies of
1062 influenza viruses. *Future Microbiol* **5**, 23-41 (2010).
1063 15. Wang, W. et al. RNA binding by the novel helical domain of the influenza virus NS1
1064 protein requires its dimer structure and a small number of specific basic amino acids.
1065 *Rna* **5**, 195-205 (1999).

1066 16. Gack, M.U. et al. Influenza A virus NS1 targets the ubiquitin ligase TRIM25 to evade
1067 recognition by the host viral RNA sensor RIG-I. *Cell Host Microbe* **5**, 439-49 (2009).
1068 17. Cecere, G. & Grishok, A. A nuclear perspective on RNAi pathways in metazoans.
1069 *Biochim Biophys Acta* **1839**, 223-33 (2014).
1070 18. Castel, S.E. & Martienssen, R.A. RNA interference in the nucleus: roles for small
1071 RNAs in transcription, epigenetics and beyond. *Nat Rev Genet* **14**, 100-12 (2013).
1072 19. La Rocca, G. & Cavalieri, V. Roles of the Core Components of the Mammalian miRISC
1073 in Chromatin Biology. *Genes (Basel)* **13**(2022).
1074 20. Nowak, I. & Sarshad, A.A. Argonaute Proteins Take Center Stage in Cancers. *Cancers*
1075 *(Basel)* **13**(2021).
1076 21. Sarshad, A.A. et al. Argonaute-miRNA Complexes Silence Target mRNAs in the
1077 Nucleus of Mammalian Stem Cells. *Mol Cell* **71**, 1040-1050.e8 (2018).
1078 22. Wang, H. et al. Altering Intracellular Localization of the RNA Interference Factors by
1079 Influenza A Virus Non-structural Protein 1. *Front Microbiol* **11**, 590904 (2020).
1080 23. Wei, W. et al. A role for small RNAs in DNA double-strand break repair. *Cell* **149**,
1081 101-12 (2012).
1082 24. Chu, Y., Yue, X., Younger, S.T., Janowski, B.A. & Corey, D.R. Involvement of
1083 argonaute proteins in gene silencing and activation by RNAs complementary to a non-
1084 coding transcript at the progesterone receptor promoter. *Nucleic Acids Res* **38**, 7736-48
1085 (2010).
1086 25. Lobo, V. et al. Loss of Lamin A leads to the nuclear translocation of AGO2 and
1087 compromised RNA interference. 2023.06.05.543674 (2023).
1088 26. Reus, J.B., Trivino-Soto, G.S., Wu, L.I., Kokott, K. & Lim, E.S. SV40 Large T Antigen
1089 Is Not Responsible for the Loss of STING in 293T Cells but Can Inhibit cGAS-STING
1090 Interferon Induction. *Viruses* **12**(2020).
1091 27. Rodriguez, L., Nogales, A. & Martinez-Sobrido, L. Influenza A Virus Studies in a
1092 Mouse Model of Infection. *J Vis Exp* (2017).
1093 28. Kosik, I. et al. Neuraminidase inhibition contributes to influenza A virus neutralization
1094 by anti-hemagglutinin stem antibodies. *J Exp Med* **216**, 304-316 (2019).
1095 29. Li, X., Gu, M., Zheng, Q., Gao, R. & Liu, X. Packaging signal of influenza A virus.
1096 *Virol J* **18**, 36 (2021).
1097 30. Ji, Z.X., Wang, X.Q. & Liu, X.F. NS1: A Key Protein in the "Game" Between Influenza
1098 A Virus and Host in Innate Immunity. *Front Cell Infect Microbiol* **11**, 670177 (2021).
1099 31. Marion, R.M., Aragon, T., Beloso, A., Nieto, A. & Ortin, J. The N-terminal half of the
1100 influenza virus NS1 protein is sufficient for nuclear retention of mRNA and
1101 enhancement of viral mRNA translation. *Nucleic Acids Res* **25**, 4271-7 (1997).
1102 32. Naceri, S., Marc, D., Camproux, A.C. & Flatters, D. Influenza A Virus NS1 Protein
1103 Structural Flexibility Analysis According to Its Structural Polymorphism Using
1104 Computational Approaches. *Int J Mol Sci* **23**(2022).
1105 33. Rouillard, A.D. et al. The harmonizome: a collection of processed datasets gathered to
1106 serve and mine knowledge about genes and proteins. *Database (Oxford)* **2016**(2016).
1107 34. Lilyestrom, W., Klein, M.G., Zhang, R., Joachimiak, A. & Chen, X.S. Crystal structure
1108 of SV40 large T-antigen bound to p53: interplay between a viral oncoprotein and a
1109 cellular tumor suppressor. *Genes Dev* **20**, 2373-82 (2006).
1110 35. Qiao, X. et al. Uncoupling DNA damage from chromatin damage to detoxify
1111 doxorubicin. *Proc Natl Acad Sci U S A* **117**, 15182-15192 (2020).
1112 36. Joerger, A.C. & Fersht, A.R. Structural biology of the tumor suppressor p53. *Annu Rev*
1113 *Biochem* **77**, 557-82 (2008).
1114 37. Schirle, N.T. & MacRae, I.J. The crystal structure of human Argonaute2. *Science* **336**,
1115 1037-40 (2012).

1116 38. Pfaff, J. et al. Structural features of Argonaute-GW182 protein interactions. *Proc Natl*
1117 *Acad Sci U S A* **110**, E3770-9 (2013).
1118 39. Gencel-Augusto, J. & Lozano, G. p53 tetramerization: at the center of the dominant-
1119 negative effect of mutant p53. *Genes Dev* **34**, 1128-1146 (2020).
1120 40. Tweddle, D.A., Malcolm, A.J., Cole, M., Pearson, A.D. & Lunec, J. p53 cellular
1121 localization and function in neuroblastoma: evidence for defective G(1) arrest despite
1122 WAF1 induction in MYCN-amplified cells. *Am J Pathol* **158**, 2067-77 (2001).
1123 41. Chen, S. et al. Arsenic Trioxide Rescues Structural p53 Mutations through a Cryptic
1124 Allosteric Site. *Cancer Cell* **39**, 225-239.e8 (2021).
1125 42. Yan, Y., Zhang, D., Zhou, P., Li, B. & Huang, S.Y. HDOCK: a web server for protein-
1126 protein and protein-DNA/RNA docking based on a hybrid strategy. *Nucleic Acids Res*
1127 **45**, W365-w373 (2017).
1128 43. Mahmoudi, S. et al. Wrap53, a natural p53 antisense transcript required for p53
1129 induction upon DNA damage. *Mol Cell* **33**, 462-71 (2009).
1130 44. Ivashkiv, L.B. & Donlin, L.T. Regulation of type I interferon responses. *Nat Rev*
1131 *Immunol* **14**, 36-49 (2014).
1132 45. Ishikawa, H. & Barber, G.N. The STING pathway and regulation of innate immune
1133 signaling in response to DNA pathogens. *Cell Mol Life Sci* **68**, 1157-65 (2011).
1134 46. Piganis, R.A. et al. Suppressor of cytokine signaling (SOCS) 1 inhibits type I interferon
1135 (IFN) signaling via the interferon alpha receptor (IFNAR1)-associated tyrosine kinase
1136 Tyk2. *J Biol Chem* **286**, 33811-8 (2011).
1137 47. Sermersheim, M. et al. MG53 suppresses interferon-β and inflammation via regulation
1138 of ryanodine receptor-mediated intracellular calcium signaling. *Nat Commun* **11**, 3624
1139 (2020).
1140 48. Pauli, E.K. et al. Influenza A virus inhibits type I IFN signaling via NF-kappaB-
1141 dependent induction of SOCS-3 expression. *PLoS Pathog* **4**, e1000196 (2008).
1142 49. Anastasakis, D.G. et al. A non-radioactive, improved PAR-CLIP and small RNA
1143 cDNA library preparation protocol. *Nucleic Acids Res* **49**, e45 (2021).
1144 50. Hauptmann, J. et al. Biochemical isolation of Argonaute protein complexes by Ago-
1145 APP. *Proc Natl Acad Sci U S A* **112**, 11841-5 (2015).
1146 51. Breuer, K. et al. InnateDB: systems biology of innate immunity and beyond--recent
1147 updates and continuing curation. *Nucleic Acids Res* **41**, D1228-33 (2013).
1148 52. Karlas, A. et al. Genome-wide RNAi screen identifies human host factors crucial for
1149 influenza virus replication. *Nature* **463**, 818-22 (2010).
1150 53. Kedzierski, L. et al. Suppressor of cytokine signaling (SOCS)5 ameliorates influenza
1151 infection via inhibition of EGFR signaling. *Elife* **6**(2017).
1152 54. Liu, Q., Chen, X., Novak, M.K., Zhang, S. & Hu, W. Repressing Ago2 mRNA
1153 translation by Trim71 maintains pluripotency through inhibiting let-7 microRNAs.
1154 *Elife* **10**(2021).
1155 55. Nguyen, D.T.T. et al. The ubiquitin ligase LIN41/TRIM71 targets p53 to antagonize
1156 cell death and differentiation pathways during stem cell differentiation. *Cell Death*
1157 *Differ* **24**, 1063-1078 (2017).
1158 56. Robinson, J.T., Thorvaldsdottir, H., Turner, D. & Mesirov, J.P. igv.js: an embeddable
1159 JavaScript implementation of the Integrative Genomics Viewer (IGV). *Bioinformatics*
1160 **39**(2023).
1161 57. Bartel, D.P. Metazoan MicroRNAs. *Cell* **173**, 20-51 (2018).
1162 58. Wang, Y. et al. Let-7 as a Promising Target in Aging and Aging-Related Diseases: A
1163 Promise or a Pledge. *Biomolecules* **12**(2022).
1164 59. Markopoulos, G.S. et al. Senescence-associated microRNAs target cell cycle regulatory
1165 genes in normal human lung fibroblasts. *Exp Gerontol* **96**, 110-122 (2017).

1166 60. Wang, L. et al. Small-Molecule Inhibitors Disrupt let-7 Oligouridylation and Release
1167 the Selective Blockade of let-7 Processing by LIN28. *Cell Rep* **23**, 3091-3101 (2018).
1168 61. Iwasaki, A. & Pillai, P.S. Innate immunity to influenza virus infection. *Nat Rev*
1169 *Immunol* **14**, 315-28 (2014).
1170 62. Wang, S. et al. AGO2 Negatively Regulates Type I Interferon Signaling Pathway by
1171 Competition Binding IRF3 with CBP/p300. *Front Cell Infect Microbiol* **7**, 195 (2017).
1172 63. Rentschler, M. et al. Nuclear Translocation of Argonaute 2 in Cytokine-Induced
1173 Senescence. *Cell Physiol Biochem* **51**, 1103-1118 (2018).
1174 64. Lobo, V. et al. Integrative transcriptomic and proteomic profiling of the effects of cell
1175 confluency on gene expression. *Sci Data* **11**, 617 (2024).
1176 65. Johnson, K.C. et al. Nuclear localization of Argonaute 2 is affected by cell density and
1177 may relieve repression by microRNAs. *Nucleic Acids Res* **52**, 1930-1952 (2024).
1178 66. Lee, S. et al. Virus-induced senescence is a driver and therapeutic target in COVID-19.
1179 *Nature* **599**, 283-289 (2021).
1180 67. Tonnessen-Murray, C.A., Lozano, G. & Jackson, J.G. The Regulation of Cellular
1181 Functions by the p53 Protein: Cellular Senescence. *Cold Spring Harb Perspect Med*
1182 **7**(2017).
1183 68. Ramos, I. et al. Innate Immune Response to Influenza Virus at Single-Cell Resolution
1184 in Human Epithelial Cells Revealed Paracrine Induction of Interferon Lambda 1. *J*
1185 *Virol* **93**(2019).
1186 69. Krell, J. et al. TP53 regulates miRNA association with AGO2 to remodel the miRNA-
1187 mRNA interaction network. *Genome Res* **26**, 331-41 (2016).
1188 70. He, F. et al. Interaction between p53 N terminus and core domain regulates specific and
1189 nonspecific DNA binding. *Proc Natl Acad Sci U S A* **116**, 8859-8868 (2019).
1190 71. tenOever, B.R. Questioning antiviral RNAi in mammals. *Nat Microbiol* **2**, 17052
1191 (2017).
1192 72. Cullen, B.R., Cherry, S. & tenOever, B.R. Is RNA interference a physiologically
1193 relevant innate antiviral immune response in mammals? *Cell Host Microbe* **14**, 374-8
1194 (2013).
1195 73. Mousavi, S.R. et al. Dysregulation of RNA interference components in COVID-19
1196 patients. *BMC Res Notes* **14**, 401 (2021).
1197 74. Adiliaghdam, F. et al. A Requirement for Argonaute 4 in Mammalian Antiviral
1198 Defense. *Cell Rep* **30**, 1690-1701.e4 (2020).
1199 75. Wang, B. et al. Influenza A Virus Facilitates Its Infectivity by Activating p53 to Inhibit
1200 the Expression of Interferon-Induced Transmembrane Proteins. *Front Immunol* **9**, 1193
1201 (2018).
1202 76. Girardi, E. et al. Cross-species comparative analysis of Dicer proteins during Sindbis
1203 virus infection. *Sci Rep* **5**, 10693 (2015).
1204 77. Zhao, N. et al. Influenza virus infection causes global RNAPII termination defects. *Nat*
1205 *Struct Mol Biol* **25**, 885-893 (2018).
1206 78. Piette, J., Neel, H. & Maréchal, V. Mdm2: keeping p53 under control. *Oncogene* **15**,
1207 1001-10 (1997).
1208 79. Whitworth, I.T. et al. Defining distinct RNA-protein interactomes of SARS-CoV-2
1209 genomic and subgenomic RNAs. 2023.05.15.540806 (2023).
1210 80. Huynh, H.T., Shcherbinina, E., Huang, H.C., Rezaei, R. & Sarshad, A.A. Biochemical
1211 Separation of Cytoplasmic and Nuclear Fraction for Downstream Molecular Analysis.
1212 *Curr Protoc* **4**, e1042 (2024).
1213 81. Jumper, J. et al. Highly accurate protein structure prediction with AlphaFold. *Nature*
1214 **596**, 583-589 (2021).

82. Ewels, P.A. et al. The nf-core framework for community-curated bioinformatics pipelines. *Nat Biotechnol* **38**, 276-278 (2020).
83. Love, M.I., Huber, W. & Anders, S. Moderated estimation of fold change and dispersion for RNA-seq data with DESeq2. *Genome Biol* **15**, 550 (2014).
84. Wang, L., Wang, S. & Li, W. RSeQC: quality control of RNA-seq experiments. *Bioinformatics* **28**, 2184-5 (2012).
85. Martin, M. Cutadapt removes adapter sequences from high-throughput sequencing reads. *2011* **17**, 3 %J EMBnet.journal (2011).
86. Corcoran, D.L. et al. PARalyzer: definition of RNA binding sites from PAR-CLIP short-read sequence data. *Genome Biol* **12**, R79 (2011).
87. Langmead, B. & Salzberg, S.L. Fast gapped-read alignment with Bowtie 2. *Nat Methods* **9**, 357-9 (2012).
88. Livak, K.J. & Schmittgen, T.D. Analysis of relative gene expression data using real-time quantitative PCR and the 2(-Delta Delta C(T)) Method. *Methods* **25**, 402-8 (2001).
89. Soubies, S.M., Volmer, C., Guerin, J.L. & Volmer, R. Truncation of the NS1 protein converts a low pathogenic avian influenza virus into a strong interferon inducer in duck cells. *Avian Dis* **54**, 527-31 (2010).
90. Baer, A. & Kehn-Hall, K. Viral concentration determination through plaque assays: using traditional and novel overlay systems. *J Vis Exp*, e52065 (2014).

1236 **FIGURES**

1237

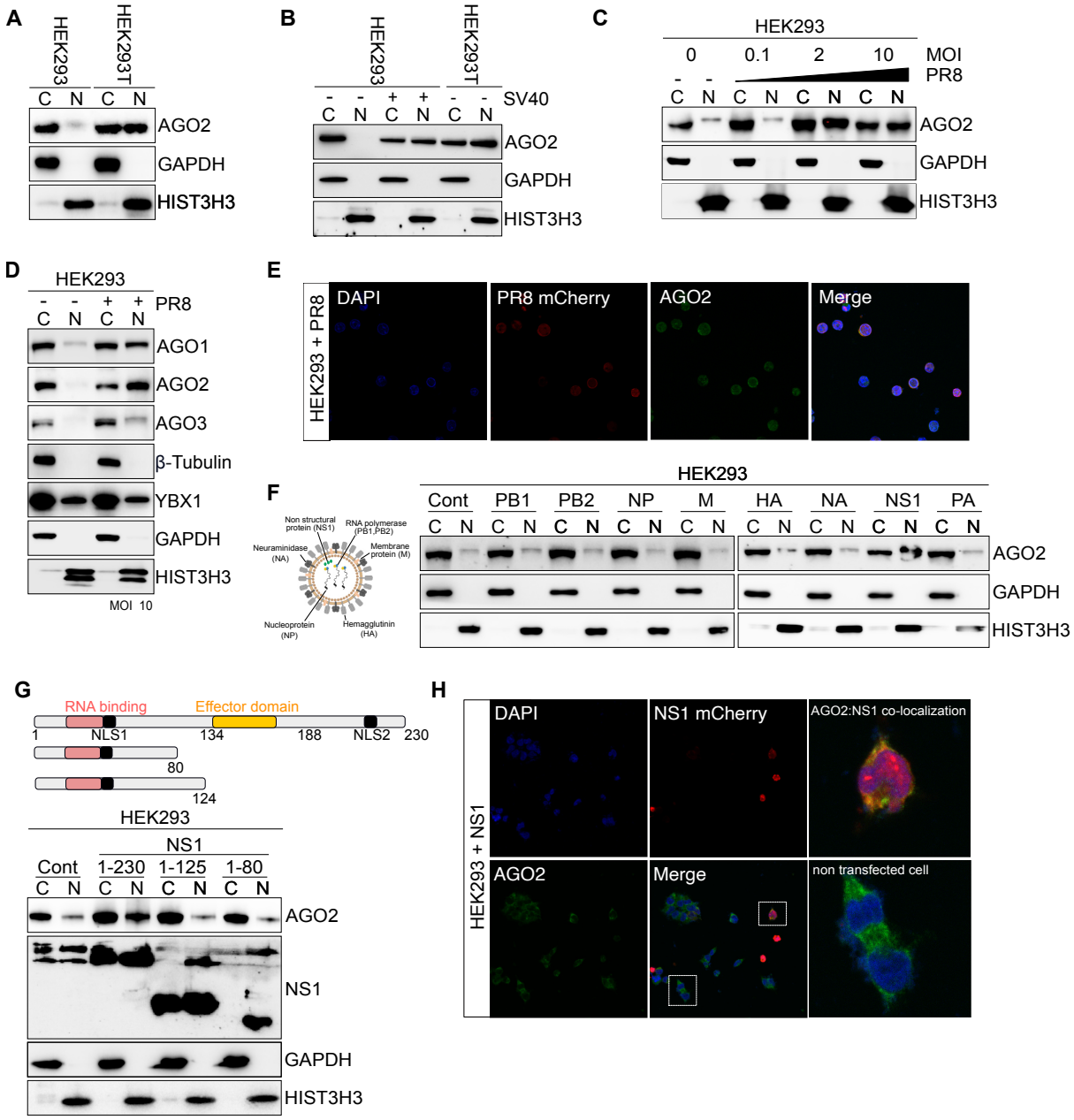

1238

1239 **Figure 1 – IAV virus NS1 induces AGO2 nuclear translocation**

1240 **(A)** Representative AGO2 immunoblots from cytoplasmic (C) and nuclear (N) lysates in
1241 HEK293 and HEK293T cells. GAPDH served as cytoplasmic marker and HIST3H3 as nuclear
1242 marker. n=3

1243 **(B)** Representative AGO2 immunoblots from cytoplasmic (C) and nuclear (N) lysates in
1244 HEK293 cells transfected with plasmid expressing SV40 Large T antigen. HEK293T was used
1245 as a positive control. GAPDH served as cytoplasmic marker and HIST3H3 as nuclear marker.
1246 n=3

1247 **(C)** Representative AGO2 immunoblots from cytoplasmic (C) and nuclear (N) lysates in
1248 HEK293 cells infected with PR8 virus at MOI 0.1; 2; 10 for 16 hours. GAPDH served as
1249 cytoplasmic marker and HIST3H3 as nuclear marker. n=3

1250 **(D)** Representative AGO1, AGO2 and AGO3 immunoblots from cytoplasmic (C) and nuclear
1251 (N) lysates in HEK293 cells infected with PR8 virus at MOI 10 for 16 hours. GAPDH and β-
1252 Tubulin served as cytoplasmic marker and HIST3H3 as nuclear marker. YBX1 served as a
1253 control for shuttling protein. n=3

1254 **(E)** Immunofluorescence images of AGO2 and PR8-mCherry in HEK293 infected with PR8-
1255 NS1-mCherry virus at MOI 10 for 16 hours. DAPI stained for DNA.

1256 **(F)** Representative AGO2 immunoblots from cytoplasmic (C) and nuclear (N) lysates in
1257 HEK293 cells transfected with PB1, PB2, NP, M, HA, NS1, and PA expressing plasmids for
1258 2 days. GAPDH served as cytoplasmic marker and HIST3H3 as nuclear marker. n=3

1259 **(G)** Representative AGO2 and NS1 immunoblots from cytoplasmic (C) and nuclear (N) lysates
1260 in HEK293 cells transfected with WT (1-230) and deletion mutant NS1 (1-80 and 1-124)
1261 expressing plasmid for 2 days. GAPDH served as cytoplasmic marker and HIST3H3 as nuclear
1262 marker. n=3

1263 **(H)** Immunofluorescence images of AGO2 and NS1-mCherry in HEK293 infected with NS1-
1264 mCherry virus at MOI 10 for 16 hours. DAPI stained for DNA. Upper box highlights a cell
1265 where AGO2 and NS1-mCherry are colocalized in the nucleus, the lower box highlights cells
1266 that were not transfected with NS1 and AGO2 remains cytoplasmic.

1267

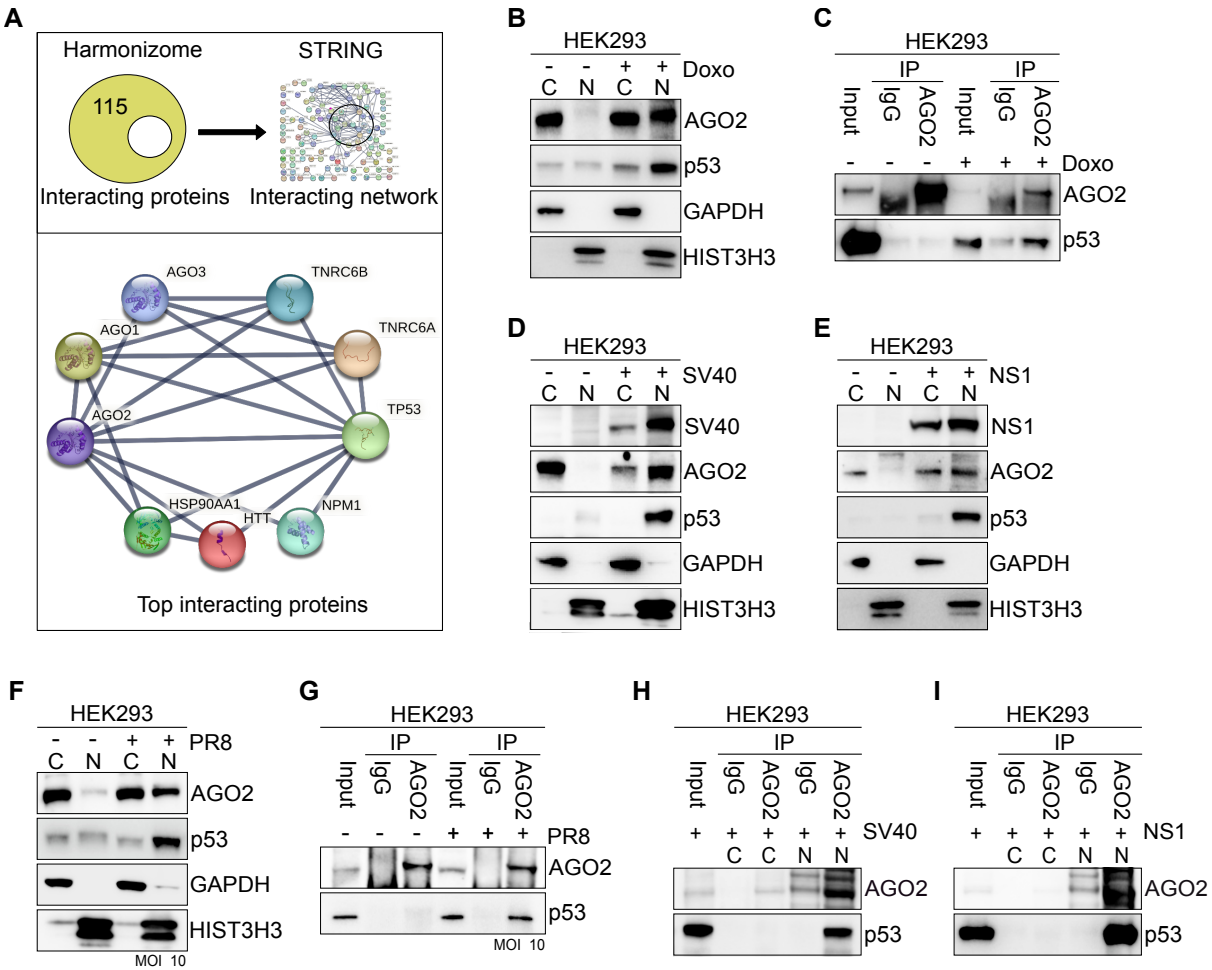

Figure 2 – p53 associates with AGO2 in the nucleus

(A) STRING protein-protein interaction network of AGO2.

(B) Representative AGO2 and p53 immunoblots from cytoplasmic (C) and nuclear (N) lysates in HEK293 cells treated with Doxorubicin (Doxo) for 24 hours. GAPDH served as a cytoplasmic marker and HIST3H3 served as nuclear marker. n=3

(C) AGO2 immunoprecipitation (IP) from HEK293 cells treated with Doxorubicin (Doxo) for 24 hours. Representative immunoblots of AGO2 and p53. n=3

(D) Representative AGO2, p53 and SV40 immunoblots from cytoplasmic (C) and nuclear (N) lysates in HEK293 cells transfected with SV40 large T antigen expressing plasmid. GAPDH served as a cytoplasmic marker and HIST3H3 served as nuclear marker. n=3

(E) same as in **(D)** except for immunoblots for NS1 in HEK293 cells transfected with NS1 mCherry expressing plasmid for 24 hours. n=3

(F) Representative AGO2 and p53 immunoblots from cytoplasmic (C) and nuclear (N) lysates in HEK293 cells infected with PR8 virus at MOI 10 for 16 hours. GAPDH served as cytoplasmic marker and HIST3H3 as nuclear marker. n=3

(G) AGO2 immunoprecipitation (IP) from HEK293 cells treated with PR8 virus at MOI 10 for 16 hours. Representative immunoblots of AGO2 and p53. n=3

1286 **(H)** AGO2 immunoprecipitation (IP) from cytoplasmic and nuclear fractions in HEK293 cells
1287 transfected with SV40 large T antigen expressing plasmid for 24 hours. Representative
1288 immunoblots of AGO2 and p53. n=3

1289 **(I)** same as in **(H)** except for HEK293 cells were transfected with WT NS1 expressing plasmid
1290 for 24 hours. n=3

1291

1292

1293

1294

1295

1296

1297

1298

1299

1300

1301

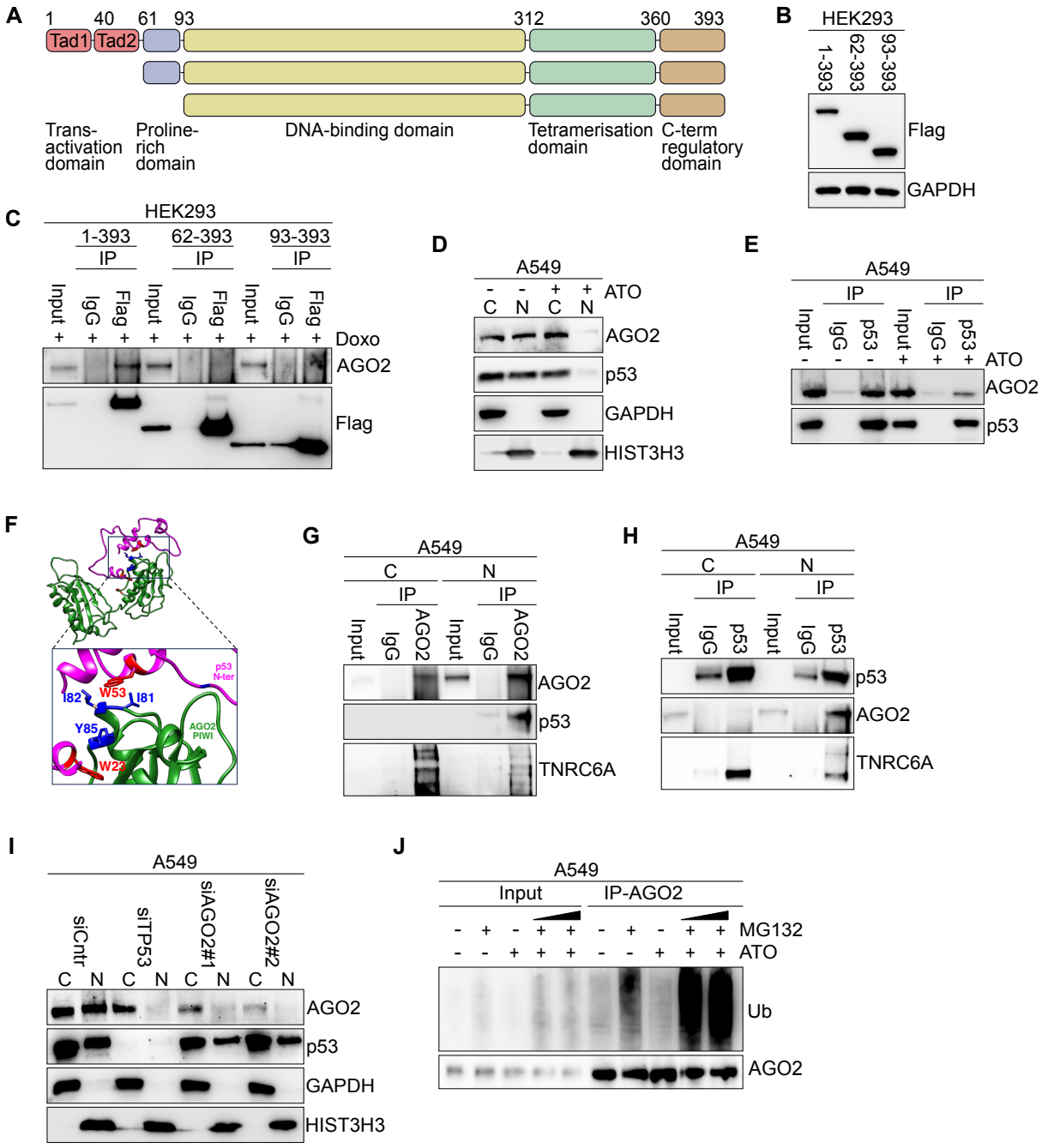

Figure 3 – Tetrameric p53 protects nuclear AGO2 from proteasomal degradation

(A) Schematic diagram of human p53 protein and N-terminal truncated Flag-tagged p53 isoforms used in the study.

(B) Representative Flag immunoblots from HEK293 cells transfected with Flag-WT-p53 or N-terminally Flag-tagged p53 mutants. GAPDH served as a loading control. n=3

(C) Flag immunoprecipitation (IP) from HEK293 cells transfected with plasmids expressing Flag-WT-p53 or N-terminally Flag-tagged p53 mutant. HEK293 cells were transfected with the p53 plasmids for 1 day and then treated with 1 μg/mL Doxorubicin (Doxo) for 1 more day. Representative immunoblots of AGO2 and Flag are indicated. n=3

1312 **(D)** Representative AGO2 and p53 immunoblots from cytoplasmic (C) and nuclear (N) lysates
1313 in A549 cells treated with 0.5 μg/mL arsenic trioxide (ATO) for 24 hours. GAPDH served as
1314 a cytoplasmic marker and HIST3H3 served as nuclear marker. n=3

1315 **(E)** p53 immunoprecipitation (IP) from A549 cells treated with 0.5 μg/mL Arsenite trioxide
1316 (ATO) for 24 hours. Representative immunoblots of AGO2 and p53. n=3

1317 **(F)** Docking model of the PIWI domain of AGO2 with the N-terminal region of p53 was
1318 generated using the HDOCK server. The PIWI domain is depicted in green, and the N-terminal
1319 region of p53 is shown in pink (model 4) in ribbon representation.

1320 **(G)** AGO2 immunoprecipitation (IP) from cytoplasmic (C) and nuclear (N) lysates in A549
1321 cells. Representative immunoblots of AGO2, p53 and TNRC6A. n=3

1322 **(H)** p53 immunoprecipitation (IP) from cytoplasmic (C) and nuclear (N) lysates in A549 cells.
1323 Representative immunoblots of AGO2, p53 and TNRC6A. n=3

1324 **(I)** Representative AGO2 and p53 immunoblots from cytoplasmic (C) and nuclear (N) lysates
1325 in A549 cells treated with siRNAs for 24 hours. siCntr: control scramble siRNAs; siTP53:
1326 siRNA specific for TP53; and siAGO2: two different siRNAs specific for AGO2. GAPDH
1327 served as a cytoplasmic marker and HIST3H3 served as nuclear marker. n=3

1328 **(J)** AGO2 immunoprecipitation (IP) from A549 cells treated with 2 μg/ml MG132 for 2 hours
1329 before additional 24 hours of treatment with 0.5 μg/ml arsenic trioxide (ATO). Representative
1330 immunoblots of ubiquitin (Ub) and AGO2. n=3

1331
1332

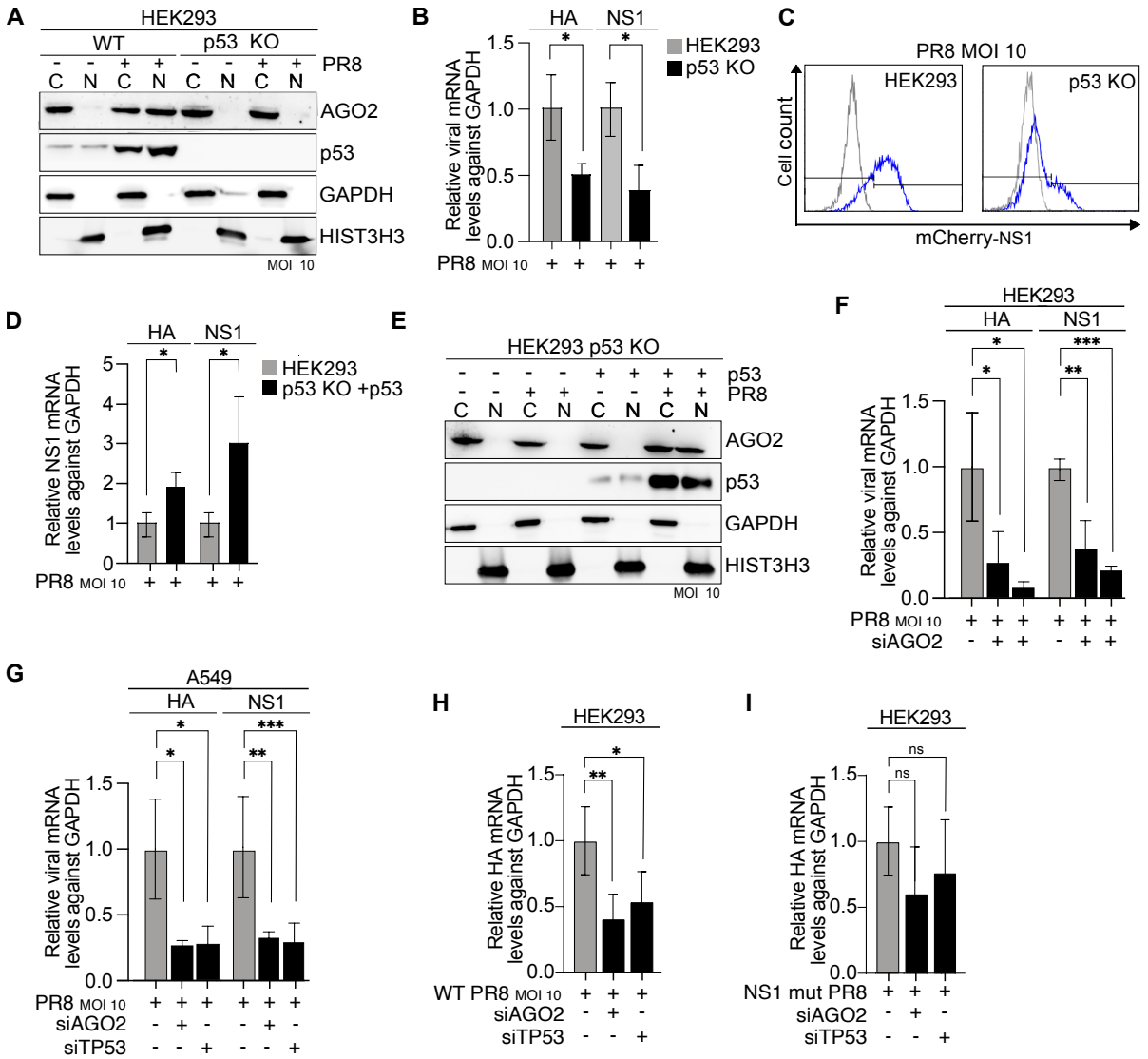

Figure 4 – Nuclear AGO2 supports viral replication

(A) Representative AGO2 and p53 immunoblots from cytoplasmic (C) and nuclear (N) lysates in WT and TP53 KO HEK293 cells infected with PR8 virus at MOI 10 for 16 hours. GAPDH served as a cytoplasmic marker and HIST3H3 served as nuclear marker. n=3

(B) Relative expression, as measured by RT-qPCR, of HA and NS1 mRNA levels in WT and TP53 KO HEK293 cells upon infection with PR8 virus at MOI 10 for 16 hours. GAPDH was used as a reference gene. Bars are mean and error bars represent ± SD. * $p<0.05$ by unpaired t-test. n=3

(C) Flow cytometry analysis of NS1-mCherry protein expression in WT and TP53 KO HEK293 cells upon infection with PR8 virus at MOI 10 for 16 hours. White histogram shows mock-infected cells while blue histogram is PR8-infected. n=3

(D) Relative expression, as measured by RT-qPCR, of HA and NS1 mRNA levels in WT and TP53 KO HEK293 cells. TP53 KO HEK293 cells were transfected with Flag-WT-p53 expressing plasmids for 24 hours. Subsequently, both TP53 KO HEK293 and TP53 KO HEK293 cells overexpressing WT p53 transiently were infected with PR8 virus at MOI 10 for

1349 16 additional hours. GAPDH was used as a reference gene. Bars are mean and error bars
1350 represent ± SD. * $p<0.05$ by unpaired t-test. n=3

1351 **(E)** Representative AGO2 and p53 immunoblots from cytoplasmic (C) and nuclear (N) lysates
1352 in TP53 KO HEK293 cells transfected with Flag-WT-p53 expressing plasmids for 24 hours
1353 and infected with PR8 virus at MOI 10 for 16 additional hours. GAPDH served as a
1354 cytoplasmic marker and HIST3H3 served as nuclear marker. n=3

1355 **(F)** Relative expression, as measured by RT-qPCR, of NS1 and HA mRNA levels in HEK293
1356 cells treated with two different siRNAs against AGO2 (siAGO2) for 48 hours. 16 hours before
1357 the end of incubation, cells were infected with PR8 virus at MOI 10. GAPDH was used as a
1358 reference gene. Bars are mean and error bars represent ± SD. * $p<0.05$, ** $p<0.01$, *** $p<0.001$
1359 by unpaired t-test. n=3

1360 **(G)** Relative expression, as measured by RT-qPCR, of NS1 and HA mRNA levels in A549
1361 cells treated with siRNAs against AGO2 (siAGO2) or TP53 (siTP53) for 48 hours. 16 hours
1362 before the end of incubation, cells were infected with PR8 virus at MOI 10. GAPDH was used
1363 as a reference gene. Bars are mean and error bars represent ± SD. * $p<0.05$, ** $p<0.01$,
1364 *** $p<0.001$ by unpaired t-test. n=3

1365 **(H)** Relative expression, as measured by RT-qPCR, of HA mRNA levels in HEK293 cells
1366 treated with siRNAs against AGO2 (siAGO2) or TP53 (siTP53) for 48 hours. 16 hours before
1367 the end of incubation, cells were infected with WT PR8 virus at MOI 10. GAPDH was used
1368 as a reference gene. Bars are mean and error bars represent ± SD. * $p<0.05$, ** $p<0.01$ by
1369 unpaired t-test. n=3

1370 **(I)** Same as in **(H)** except cells were infected with PR8 virus expressing mutant NS1 at MOI
1371 10 were. n=3

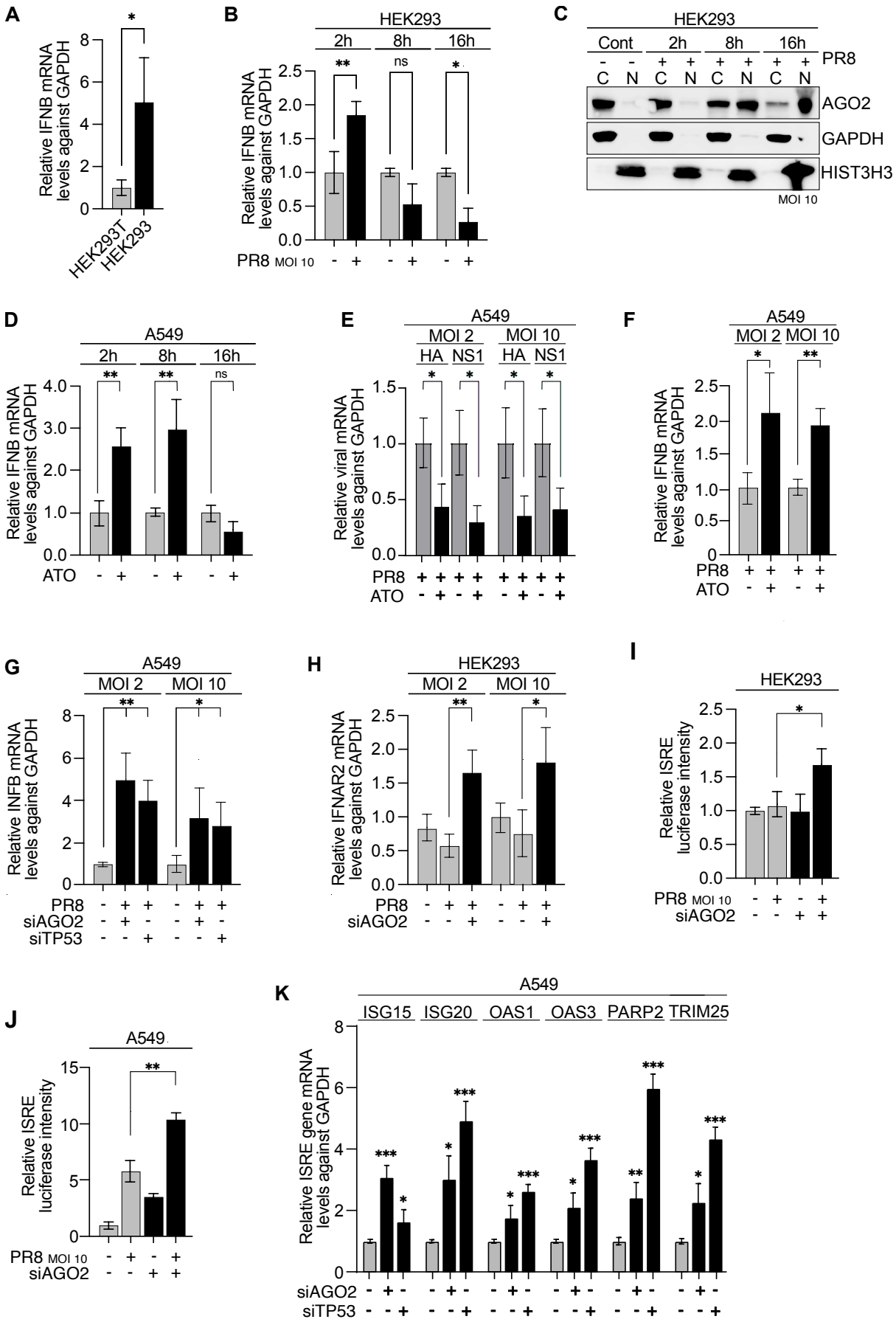

Figure 5 – Nuclear AGO2 downregulates *IFNB* and other type-I-IFN related genes

1374 **(A)** Relative expression, as measured by RT-qPCR, of IFNB mRNA levels in HEK293T and
1375 HEK293 cells. GAPDH was used as a reference gene. Bars are mean and error bars represent
1376 ± SD. * $p<0.1$ by unpaired t-test. n=3

1377 **(B)** Relative expression, as measured by RT-qPCR, of IFNB mRNA levels in HEK293 cells
1378 infected with PR8 virus at MOI 10 for 2, 8 or 16 hours. GAPDH was used as a reference gene.
1379 Bars are mean and error bars represent ± SD. * $p<0.05$, ** $p<0.01$ by unpaired t-test. n=3

1380 **(C)** Representative AGO2 immunoblots from cytoplasmic (C) and nuclear (N) lysates in
1381 HEK293 cells infected with PR8 virus at MOI 10 for 2, 8 or 16 hours. GAPDH served as a
1382 cytoplasmic marker and HIST3H3 served as nuclear marker. n=3

1383 **(D)** Relative expression, as measured by RT-qPCR, of IFNB mRNA levels in A549 cells
1384 treated with 0.5 µg/mL arsenic trioxide (ATO) for 2, 8 or 16 hours. GAPDH was used as a
1385 reference gene. Bars are mean and error bars represent ± SD. ** $p<0.01$ by unpaired t-test. n=3

1386 **(E)** Relative expression, as measured by RT-qPCR, of HA and NS1 mRNA levels in A549
1387 cells treated for 2 hours with 0.5 µg/ml arsenic trioxide (ATO)) or vehicle and infected with
1388 PR8 virus at MOI 2 or MOI 10 for 16 hours. GAPDH was used as a reference gene. Bars are
1389 mean and error bars represent ± SD. * $p<0.05$ by unpaired t-test. n=3

1390 **(F)** same as in **(E)** but IFNB mRNA level were measured by RT-qPCR. n=3

1391 **(G)** Relative expression, as measured by RT-qPCR, of IFNB mRNA levels in A549 cells
1392 treated with siRNAs against TP53 or AGO2 for 48 hours. 16 hours before the end of incubation,
1393 cells were infected with PR8 virus at MOI 2 or MOI 10. GAPDH was used as a reference gene.
1394 Bars are mean and error bars represent ± SD. *** $p<0.001$, **** $p<0.0001$ by unpaired t-test. n=3

1395 **(H)** Relative expression, as measured by RT-qPCR, of IFNAR2 mRNA levels in HEK293 cells
1396 treated with siRNA against AGO2 for 48 hours. 16 hours before the end of incubation, cells
1397 were infected with PR8 virus at MOI 2 or MOI 10. GAPDH was used as a reference gene.
1398 Bars are mean and error bars represent ± SD. * $p<0.05$ by unpaired t-test. n=3

1399 **(I)** Normalized lucifersase signal of ISRE-transfected HEK293 cells, treated with siRNA
1400 against AGO2 for 48 hours. 16 hours before the end of incubation, cells were infected with
1401 PR8 virus at MOI 10. GAPDH was used as a reference gene. Bars are mean and error bars
1402 represent ± SD. * $p<0.05$ by unpaired t-test. n=3

1403 **(J)** same as in **(I)** but in A549 cells. n=3

1404 **(K)** Relative expression, as measured by RT-qPCR, of ISG15, ISG20, OAS1, OAS3,
1405 PARRP12, and TRIM25 mRNA levels A549 cells treated with siRNA against AGO2 for 48
1406 hours. 16 hours before the end of incubation, cells were infected with PR8 virus at MOI 10.
1407 GAPDH was used as a reference gene. Bars are mean and error bars represent ± SD. * $p<0.05$
1408 by unpaired t-test. n=3

1409

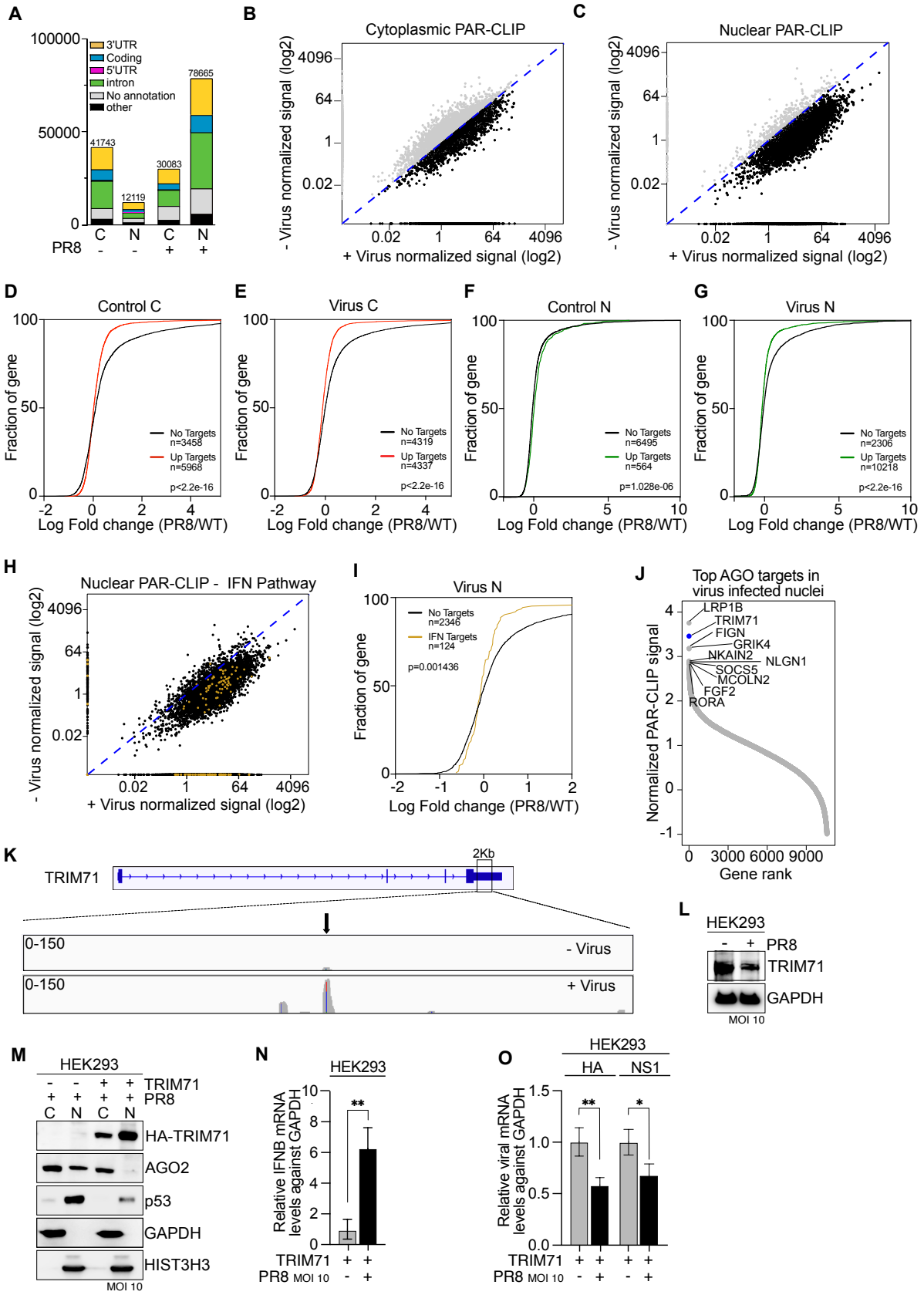

Figure 6 – Nuclear AGO2 downregulates type-I IFN pathway genes and TRIM71 in IAV-infected cells

1413 **(A)** Distribution of fPAR-CLIP sequence reads in clusters across target RNA across 3′UTR,
1414 coding sequence, 5′UTR, and introns from cytoplasmic (C) and nuclear (N) fractions of
1415 HEK293 cells infected with PR8 virus at MOI 10 for 16 hours. The graph shows the average
1416 of 2 independent experiments.

1417 **(B)** Scatter plot of cytoplasmic fPAR-CLIP log2 normalized signal in control (- Virus) and
1418 IAV infected (+Virus) HEK293 cells. Each dots represents a gene and is the average of 2
1419 independent experiments. Blue dashed line shows a perfect correlation. Black dots are genes
1420 with higher PAR-CLIP signal in the IAV-infected sample while grey dots are genes with higher
1421 PAR-CLIP signal in the control sample.

1422 **(C)** same as in **(B)** but for nuclear fPAR-CLIP.

1423 **(D)** Cumulative distribution function of AGO1-4 targets in control cytoplasmic fraction
1424 compared to non-targets. Targets are the genes depicted as grey dots in (**B**)

1425 **(E)** Cumulative distribution function of AGO1-4 targets in virus infected cytoplasmic fraction
1426 compared to non-targets. Targets are the genes depicted as black dots in (**B**)

1427 **(F)** Cumulative distribution function of AGO1-4 targets in control nuclear fraction compared
1428 to non-targets. Targets are the genes depicted as grey dots in (**C**)

1429 **(G)** Cumulative distribution function of AGO1-4 targets in virus infected nuclear fraction
1430 compared to non-targets. Targets are the genes depicted as black dots in (**C**)

1431 **(H)** same graph as in **(C)** but with type-I IFN pathway genes highlighted in golden yellow.

1432 **(I)** same as in **(G)** but for type-I IFN pathway genes.

1433 **(J)** Rank plot showing AGO targets, ordered by normalized PAR-CLIP signal, in IAV infected,
1434 nuclear fraction of HEK293 cells. Each dot represents a gene and is the average of 2
1435 independent experiments.

1436 **(K)** TRIM71 IGV track in nuclear fraction of in control (- Virus) and IAV infected (+Virus)
1437 HEK293 cells.

1438 **(L)** Representative TRIM71 immunoblots from whole cell lysates in HEK293 infected with
1439 PR8 virus at MOI 10 for 16 hours. GAPDH served as a loading control. n= 3

1440 **(M)** Representative HA-TRIM71, AGO2 and p53 immunoblots from cytoplasmic (C) and
1441 nuclear (N) lysates in HEK293 cells transfected with HA-TRIM71 and infected with PR8 virus
1442 at MOI 10 for 16 hours. GAPDH served as a cytoplasmic marker and HIST3H3 served as
1443 nuclear marker. n= 3

1444 **(N)** Relative expression, as measured by RT-qPCR, of IFNB mRNA levels in HEK293 cells
1445 transfected with HA-TRIM71 and infected with PR8 virus at MOI 10 for 16 hours. GAPDH
1446 was used as a reference gene. Bars are mean and error bars represent ± SD. ∗∗ $p<0.01$ by
1447 unpaired t-test. n= 3

1448 **(O)** Relative expression, as measured by RT-qPCR, of HA and NS1 mRNA levels in HEK293
1449 cells transfected with HA-TRIM71 and infected with PR8 virus at MOI 10 for 16 hours.

GAPDH was used as a reference gene. Bars are mean and error bars represent ± SD. ∗ $p<0.05$, ∗∗ $p<0.01$ by unpaired t-test. n= 3

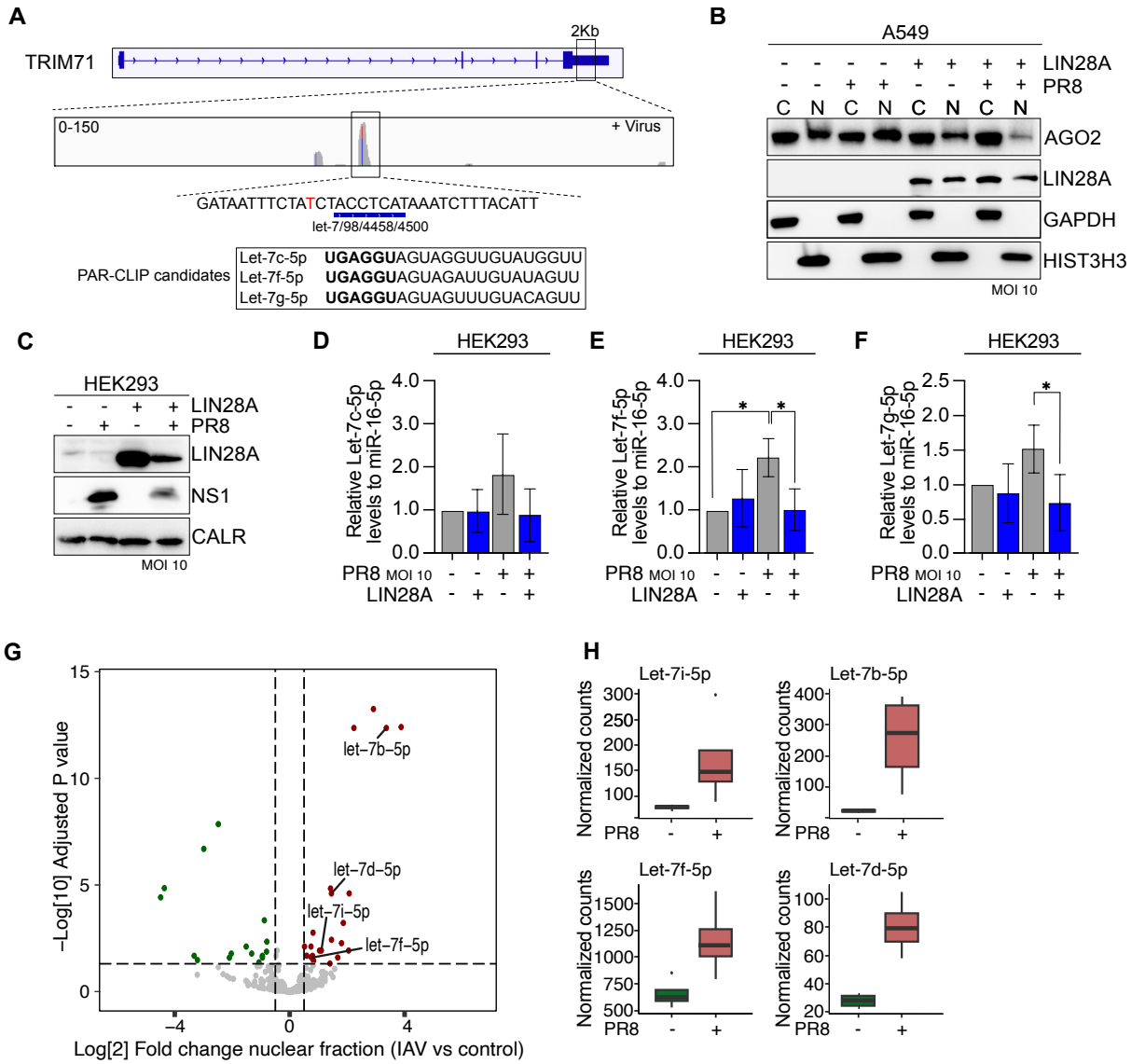

Figure 7. Let-7 miRNA, targeting TRIM71, are upregulated in the nucleus of IAV-infected cells

(A) TRIM71 IGV track in nuclear fraction of in IAV infected (+Virus) HEK293 cells. Indicated is the TRIM71 sequence, predicted Let-7 seed sequence and Let-7 PAR-CLIP targets.

(B) Representative AGO2 and LIN28A immunoblots from cytoplasmic (C) and nuclear (N) lysates in A549 cells transfected with LIN28A expressing plasmid and infected with PR8 virus at MOI 10 for 16 hours. GAPDH served as a cytoplasmic marker and HIST3H3 served as nuclear marker. n=3

(C) Representative LIN28A and NS1 immunoblots from cytoplasmic (C) and nuclear (N) lysates in HEK293 cells transfected with LIN28A expressing plasmid and infected with PR8 virus at MOI 10 for 16 hours. CALR served as a loading control. n=3

(D) Relative expression, as measured by RT-qPCR, of Let-7c-5p RNA levels in HEK293 cells transfected with V5-LIN28A expressing plasmid and infected with PR8 virus at MOI 10 for

1485 16 hours. miR-16-5p was used as a reference gene. Bars are mean and error bars represent ±
1486 SD. n= 3

1487 **(E)** same as in **(D)** but for Let-7f-5p RNA. Bars are mean and error bars represent ± SD. ∗
1488 $p<0.05$ by unpaired t-test. n= 3

1489 **(F)** same as in **(D)** but for Let-7g-5p RNA. Bars are mean and error bars represent ± SD. ∗
1490 $p<0.05$ by unpaired t-test. n= 3

1491 **(G)** Volcano plot showing miRNAseq results of differentially expressed miRNAs from the
1492 nuclear fraction of PR8 infected and non infected HEK293 cells. In red are the upregulated
1493 genes while in green the downregulated.

1494 **(H)** Significantly differentially expressed Let7i/b/f/d-5p from the nuclear fraction of PR8
1495 infected and non infected HEK293 cells.

1496

1497

1498
1499
1500

1501

1502

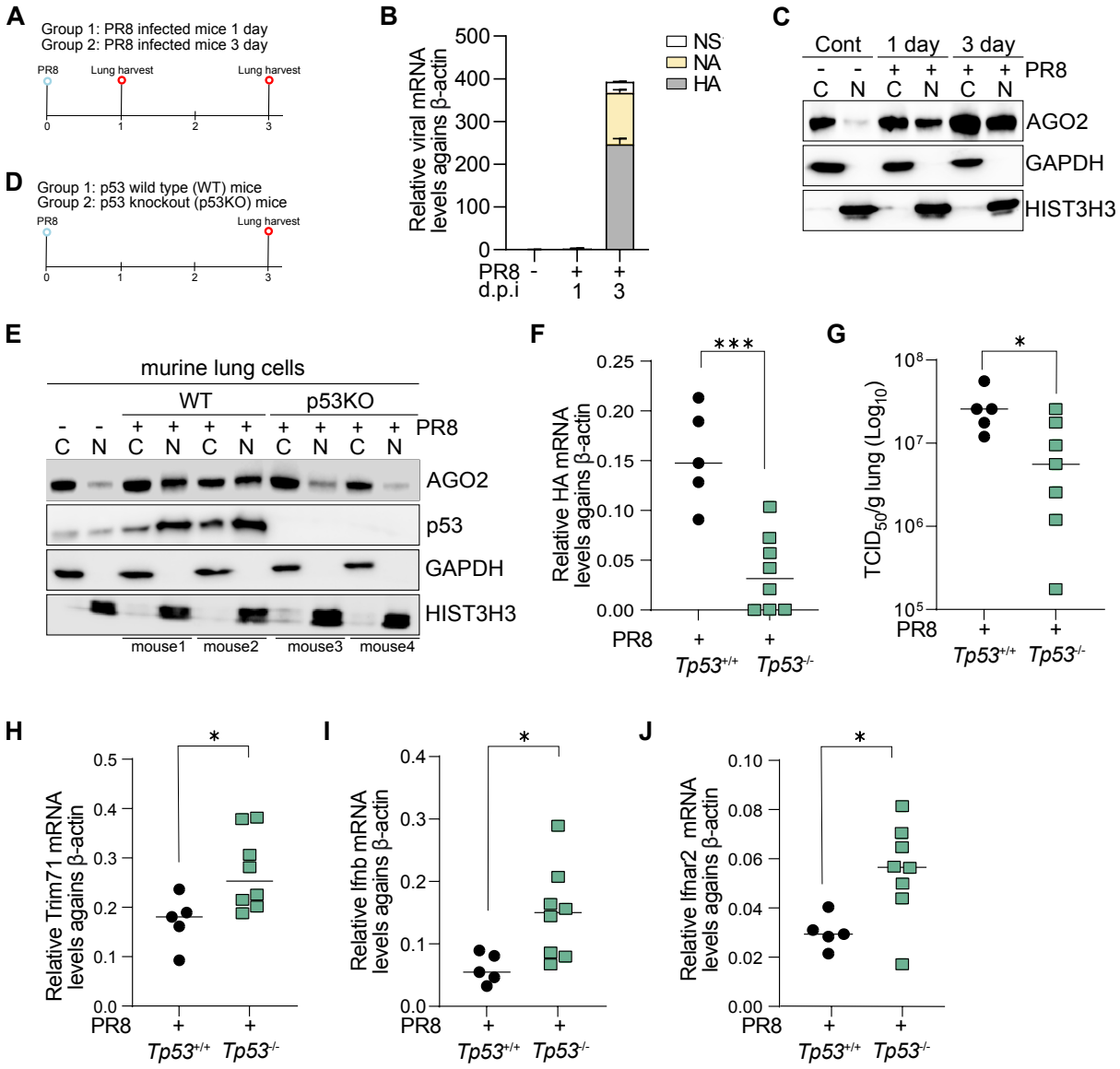

Figure 8 – p53/AGO2 axis contributes to the decrease in IFN-related genes and increased viral titers *in vivo*.

(A) Schematic representation of the experimental setup for experiments in **(B)** and **(C)**. Mice were infected i.n. with 2000 $TCID_{50}$ PR8 at day 0 and lungs harvested at 1 and 3 days post-infection.

(B) Relative expression, as measured by RT-qPCR, of NS1 and HA mRNA levels in lung cells isolated from mice at 1 or 3 days post-infection. β-actin was used as a reference gene. Error bars represent ± SD.

(C) Representative AGO2 immunoblots from cytoplasmic (C) and nuclear (N) lysates in lung cells isolated from mice at 1 or 3 days post-infection. GAPDH served as a cytoplasmic marker and HIST3H3 served as nuclear marker. n= 2 independent experiments with 2 mice each

(D) Schematic representation of the experimental setup for experiments in **(E-J)**. WT and *Tp53-/-* mice were infected i.n. with 2000 $TCID_{50}$ PR8 and lungs harvested at 3 days post-infection.

1518 **(E)** Representative Ago2 and p53 immunoblots from cytoplasmic (C) and nuclear (N) lysates
1519 in lung cells isolated from WT and *Tp53*$^{-/-}$ mice infected with PR8. GAPDH served as a
1520 cytoplasmic marker and HIST3H3 served as nuclear marker. n=1 independent experiments
1521 with a total of 5 WT and 8 *Tp53*$^{-/-}$ mice.

1522 **(F)** Graph representing HA mRNA levels in lung cells isolated from WT and *Tp53*$^{-/-}$ mice
1523 infected with PR8. Shown are the individual mice with bar respresenting the mean and error
1524 bars represent ± SD. *** $p<0.001$ by unpaired t-test. n=1 independent experiments with a total
1525 of 5 WT and 8 *Tp53*$^{-/-}$ mice.

1526 **(G)** Graph representing $\log_{10}$ $TCID_{50}$/g lung in WT and *Tp53*$^{-/-}$ mice with PR8 infection. Shown
1527 are the individual mice with bar respresenting the mean and error bars represent ± SD. * $p<0.05$
1528 by unpaired t-test. n=1 independent experiments with a total of 5 WT and 8 *Tp53*$^{-/-}$ mice.

1529 **(H)** Graph representing the mRNA levels of *Trim71* in lung cells isolated from WT and *Tp53*$^{-}$
1530 $^{/-}$ mice with PR8 infection. Shown are the individual mice with bar respresenting the mean and
1531 error bars represent ± SD. * $p<0.05$ by unpaired t-test. n=1 independent experiments with a
1532 total of 5 WT and 8 *Tp53*$^{-/-}$ mice.

1533 **(I)** same as in **(H)** but for *Ifnb.* * $p<0.05$ by unpaired t-test.

1534 **(J)** same as in **(H)** but for *Ifnar2.* * $p<0.05$ by unpaired t-test